Observation-Based Estimates of Water Mass Transformation and Formation in the Labrador Sea

SIJIA ZOU,[a] TILLYS PETIT,[b] FEILI LI,[a] AND M. SUSAN LOZIER[c]

[a] *State Key Laboratory of Marine Environmental Science and College of Ocean and Earth Sciences, Xiamen University, Xiamen, China*
[b] *National Centre for Atmospheric Science, Department of Meteorology, University of Reading, Reading, United Kingdom*
[c] *School of Earth and Atmospheric Science, Georgia Institute of Technology, Atlanta, Georgia*

(Manuscript received 20 November 2023, in final form 9 March 2024, accepted 10 April 2024)

ABSTRACT: The water mass produced during wintertime convection in the Labrador Sea [i.e., the Labrador Sea Water (LSW)] is characterized by distinct thermohaline properties. It has been shown to exert a critical impact on the property and circulation fields of the North Atlantic. However, a quantitative understanding of the transformation and formation processes that produce LSW is still incomplete. Here, we evaluate the mean water mass transformation (WMT) and formation rates in the Labrador Sea, along with their forcing attributions, in both density and thermohaline coordinates using observation-based datasets during 2014–19. We find that while surface buoyancy loss results in an expected densification of the basin and thus LSW formation, interior mixing has an indispensable and more complex impact. In particular, mixing across density surfaces is estimated to account for 63% of the mean formation rate in the LSW layer [4.9 Sv (1 Sv ≡ 10^6 m^3 s^{-1})] and does so by converting both upper-layer and overflow layer waters into the LSW layer. In addition, mixing along density surfaces is shown to be responsible for the pronounced diathermohaline transformation (~10 Sv) west of Greenland. This is the primary process through which the cold and fresh LSW in the basin interior is exchanged with the warm and salty Irminger Water in the boundary current. Results from this study underline the critical role of mixing (both across and along density surfaces) in determining the volume and properties of the LSW, with implications for better understanding and simulating deep-water evolution under climate change.

KEYWORDS: Mass fluxes/transport; Meridional overturning circulation; Mixing

1. Introduction

The Labrador Basin, a semienclosed basin in the northwestern North Atlantic (Fig. 1), is one of the few locations in the global ocean where deep convection occurs (Marshall and Schott 1999). Cold air outbreaks during winter remove buoyancy from the weakly stratified water column, triggering convective mixing to depths of 1000–2000 m (Lazier et al. 2002; Yashayaev 2007; Yashayaev and Loder 2017). During convection, the deep ocean becomes ventilated and sequestrates carbon and oxygen from the atmosphere, with important implications for global climate change and marine biological activities (Sabine et al. 2004; Pérez et al. 2013; Koelling et al. 2017). The product of convective mixing is the Labrador Sea Water (LSW), an intermediate-depth water mass with characteristically low salinity, low potential vorticity, and high oxygen content (Fig. 2; Talley and McCartney 1982; Koelling et al. 2017). After formation, LSW is exported from the Labrador Basin to the other subpolar basins, as well as equatorward as part of the lower limb of the Atlantic meridional overturning circulation (AMOC).

Many modeling and paleoceanographic studies have stressed the importance of the Labrador Sea convection to the AMOC transport, with enhanced convection leading to a strengthened AMOC on decadal and longer time scales (Biastoch et al. 2008; Danabasoglu et al. 2012; Thornalley et al. 2018; Zhang et al. 2019; Li et al. 2019; Yeager et al. 2021). For example, according to sensitivity experiments in a suite of ocean circulation models (1/2°–1/12°), Biastoch et al. (2008) have shown that positive AMOC anomalies emerge 1–2 years after the onset of intensified LSW production on decadal time scales. However, estimates of the overturning in the Labrador Sea based on hydrographic transects are quite small [2–5 Sv (1 Sv ≡ 10^6 m^3 s^{-1}); Pickart and Spall 2007; Hall et al. 2013], even in the early 1990s when intensified convection occurred. More recently, direct moored measurements from the Overturning in the Subpolar North Atlantic Program (OSNAP) have shown that the overturning east of Greenland (15–17 Sv) far outweighs the contribution from the Labrador Sea since 2014 (2–3 Sv; Lozier et al. 2019; Li et al. 2021; Fu et al. 2023), another period with intensified convection (Yashayaev and Loder 2017). Collectively, these observation-based studies suggest an overall weak overturning response to convection in the Labrador Sea. The discrepancy between models and observations may be attributed to the common salinity biases in models that significantly impact the simulated density structure in the basin

---

Denotes content that is immediately available upon publication as open access.

Supplemental information related to this paper is available at the Journals Online website: https://doi.org/10.1175/JPO-D-23-0235.s1.

Petit's current affiliation: National Oceanography Center, Southampton, United Kingdom.

Corresponding author: Sijia Zou, szou@xmu.edu.cn

DOI: 10.1175/JPO-D-23-0235.1

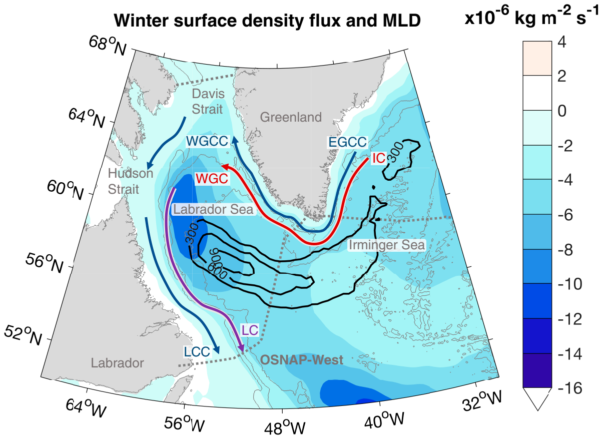

FIG. 1. Winter air–sea density flux in the Labrador Sea. Negative values indicate a density flux from the atmosphere to the ocean, meaning that the ocean is gaining density (or losing buoyancy). Data are obtained by averaging the monthly density fluxes during winter months (January–March) from 2015 to 2019 among the combination of three atmospheric reanalysis datasets (section 2d). Black contours represent winter mixed layer depths averaged among three oceanic datasets on a regular grid of 1/2° (section 2c). The mixed layer depth is defined using a density threshold method (de Boyer Montégut et al. 2004). Specifically, it is estimated as the depth at which potential density exceeds that at 10 m by 0.01 kg m^{-3}. The OSNAP West section is indicated as a dotted gray line. Major boundary currents are illustrated with arrows, including the East Greenland Coastal Current (EGCC), Irminger Current (IC), West Greenland Coastal Current (WGCC), WGC, Labrador Coastal Current (LCC), and the LC. The 1000-, 2000-, and 3000-m from ETOPO2 are contoured in light gray.

and therefore the overturning strength (Jackson and Petit 2023; Zou et al. 2020a). On the other hand, the Labrador Sea convection may have remote and delayed impacts on the AMOC that are not captured by the observational time scales. For example, using a high-resolution ocean circulation model (1/20°), Böning et al. (2023) suggest that enhanced convection may contribute to overturning east of Greenland by the spreading and entrainment of the dense LSW into the Irminger Sea.

In steady state, the overturning transport in density coordinate along a section equals the diapycnal (i.e., across density surface) volume flux (or the diapycnal transformation) within the basin enclosed by the section and the coastal boundaries (Walin 1982; Speer and Tziperman 1992; Marsh 2000; Grist et al. 2010). Thus, an alternative way to evaluate the contribution of Labrador Sea convection to the AMOC is to estimate the diapycnal volume flux in the basin. A number of studies have estimated the diapycnal transformation induced by air–sea buoyancy flux in the North Atlantic (Speer et al. 1995; Marsh 2000; Myers and Donnelly 2008; Grist et al. 2009, 2014; Desbruyeères et al. 2019). In particular, using an atmospheric reanalysis product, Petit et al. (2020) calculated the mean surface-induced diapycnal transformation during August 2014–May 2016 in the Labrador Sea, which was 1.5 ± 0.7 Sv at σ_θ =27.70 kg m^{-3}. This number compares favorably to the overturning transport at the same isopycnal over the same time period (2.1 ± 0.3 Sv; Petit et al. 2020) along OSNAP West (Fig. 1), suggesting a dominant role of surface forcing in transforming dense waters that compose the overturning circulation. However, given the short time period considered and the level of uncertainty, it is possible that the system is not in steady state, and other processes, such as diapycnal mixing, play a role.

What is also uncertain is the formation rate of the LSW density layer (see Haine et al. 2008 and Garcia-Quintana et al. 2019 for reviews) and its forcing attributions. Previous estimates using different approaches, including those based on chlorofluorocarbon inventories (Smethie and Fine 2001; Rhein et al. 2002; LeBel et al. 2008), air–sea flux calculations (Speer and Tziperman 1992; Marsh 2000; Khatiwala et al. 2002; Myers and Donnelly 2008), numerical models (Böning et al. 1996; Marsh et al. 2005; Garcia-Quintana et al. 2019; Yeager et al. 2021), and inverse methods (Mackay et al. 2020), vary significantly—from 2 to 11 Sv. In addition to the distinct methods used, this large range may also be attributed to the inconsistent definitions of the density range of the LSW layer and the different time periods considered among the studies. Estimates based on numerical simulations are also sensitive to the model resolution and configuration (Garcia-Quintana et al. 2019). In fact, as pointed out by Haine et al. (2008), many studies did not provide uncertainty estimates for LSW layer formation rates, making it difficult to draw a robust conclusion. Furthermore, past studies mostly focused on formation in response to surface buoyancy forcing. However, OSNAP observations have suggested a possible conversion of the overflow layer waters into the LSW layer (Zou et al. 2020a), probably induced by mixing, which adds another possible forcing mechanism for LSW formation.

So far, much of the attention on transformation and formation has been paid on the diapycnal processes because of their direct linkage to the overturning circulation in density space. However, water masses may experience important thermohaline changes with compensating impacts on density, which cannot be illustrated by density coordinate. For example, using the 21-month observations at OSNAP West, Zou et al. (2020a) reported that the mean maximum diathermal (i.e., across temperature surface) and diahaline (i.e., across salinity surface) transformations were 11–14 Sv, about 3–4 times greater than the maximum diapycnal transformation (3 Sv) in the Labrador Sea, suggesting significant density compensation by the thermal and haline anomalies. The strong diathermal and diahaline transformations are reflected by the stark contrasts in temperature and salinity between the inflow and outflow across the upper Labrador Sea. As shown in Fig. 2, relatively warm and salty Irminger Water (IW) flows into the basin at ~500 m via the West Greenland Current (WGC; Pacini et al. 2020). By the time the boundary current exits the basin, where it is known as the Labrador Current (LC), it becomes much colder and fresher. This property change has been attributed to the lateral exchange of heat and salt between the boundary current and the basin interior (Cuny et al. 2002; de Jong et al. 2014, 2016), as well as to the convective overturning that takes place within the boundary in response

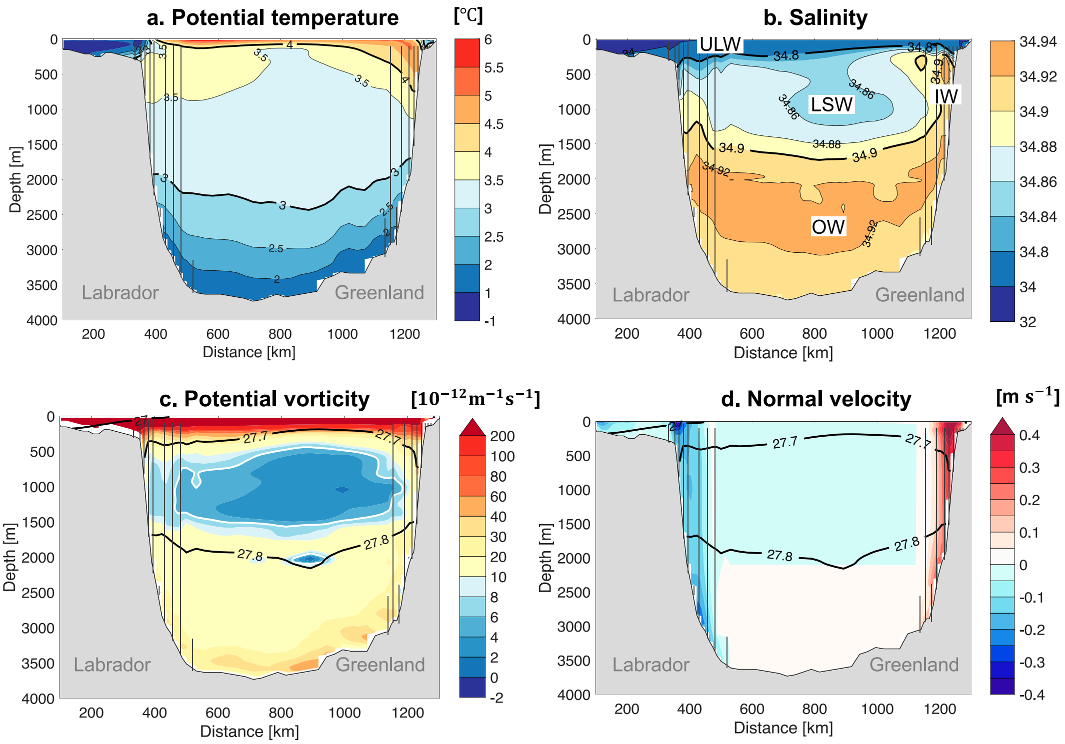

FIG. 2. (a) Mean potential temperature and (b) mean salinity at the OSNAP West section during August 2014–August 2019. Isotherms and isohalines are contoured in black. Major water masses are labeled, including the ULW, LSW, IW, and OW. Definitions of these water masses are described in section 2e. (c) Mean planetary potential vorticity [i.e., $f(N^2/g)$, where N^2 is the buoyancy frequency]. The white contour encloses area where potential vorticity is smaller than $6 \times 10^{-12}\mathrm{m}^{-1}\mathrm{s}^{-1}$. Potential densities σ_θ, referenced to the sea surface, of 27, 27.7, and 27.8 kg m^{-3} are contoured in black. (d) Mean velocity normal to the section. Positive values indicate flow into the basin. In all plots, vertical lines represent OSNAP mooring locations.

to surface buoyancy loss (Pickart et al. 1997, 2002; Brandt et al. 2007; Palter et al. 2008; MacGilchrist et al. 2020). In particular, the boundary convective overturning may directly bring surface fresh and cold waters of Arctic/Greenland origin down to a few hundreds of meters, resulting in thermohaline anomalies in the boundary current. Using an idealized simulation, a recent study has shown that the cold and fresh anomalies in the boundary current can be attributed to surface heat loss for the former and mixing with freshwater along the Greenland and Labrador shelves for the latter (Bebieva and Lozier 2023). Lacking from these studies is an analysis of observational data that quantitatively links each possible forcing mechanism to the diathermohaline (i.e., across temperature and salinity surfaces) volume fluxes.

The diagnostic framework for water mass transformation (WMT) and formation in thermohaline coordinates has been developed and applied both globally and regionally (Groeskamp et al. 2014a,b; Mackay et al. 2018, 2020; Evans et al. 2014, 2023). This framework establishes an unambiguous linkage between the velocity field and the thermohaline forcing that includes surface heat and freshwater fluxes, as well as diffusive heat and salt fluxes in the interior (Groeskamp et al. 2014a). Thus, the framework is particularly useful in understanding the driving mechanisms for the diathermohaline volume fluxes. For example, using observational and ocean reanalysis datasets, Mackay et al. (2020) and Evans et al. (2023) evaluated volume fluxes in thermohaline coordinates in an extended region from the subpolar North Atlantic to the Bering Strait and revealed the respective role of surface heat flux and interior mixing in driving the thermohaline changes in this area.

With a focus on the Labrador Sea, the goals of this study are to estimate the water mass transformation and formation rates in both density and thermohaline coordinates and to assess their quantitative attributions to the thermohaline forcing from an observational perspective. To this end, we combine moored measurements at OSNAP West and the Davis Strait, gridded hydrographic datasets, and atmospheric reanalysis products to conduct volume budget analysis in both density and thermohaline coordinates during the time period from August 2014 to August 2019.

2. Data and methods

a. *Moored measurements at OSNAP West*

Monthly gridded temperature, salinity, and velocity data along the OSNAP West section from August 2014 to August 2019 are used in this study (Fu et al. 2023). This time period is chosen since it covers five full seasonal cycles during the OSNAP observational period. It is worth noting that our study period follows intense convective activity in the winters of 2014–16 (Yashayaev and Loder 2017) and thus offers the opportunity to evaluate water mass changes associated with strong convection. The OSNAP product are obtained by objective analysis that incorporates various sources of data, including mooring measurements mainly within the boundary currents (Fig. 2), Argo profiles, satellite altimetry, shipboard hydrographic transects, and *World Ocean Atlas* climatology. The horizontal resolution is <25 km, and the vertical resolution is 20 m. The gridded velocity field at OSNAP West allows for a net transport of -1.6 ± 0.2 Sv across the section to account for the southward throughflow across the Davis Strait (section 2b). More information about the OSNAP data and methodology can be found in Lozier et al. (2019) and Li et al. (2017, 2021).

b. *Moored measurements at the Davis Strait*

At the Davis Strait, which is the northern boundary of the Labrador Basin (Fig. 1), we use the monthly objectively mapped product from the Davis Strait observing system (Curry et al. 2014). The product contains salinity, temperature, and along-strait velocity measured by moorings and seagliders across the strait between Baffin Island and Greenland. The horizontal resolution of the gridded product varies from 1 to 8 km, and the vertical resolution is 4 m in the upper 370 and 10 m at greater depths. Unfortunately, the temporal span of the data, which is from 2004 to 2010, does not overlap with the time period of the OSNAP measurements. Here, we assume that the multiyear averaged transport during 2004–10 is representative of the mean over the OSNAP time period at the Davis Strait. This assumption and its limitations should be kept in mind when considering the results presented in this study. As shown in Fig. S1 in the online supplemental material, the mean volume transport through the Davis Strait is -1.6 Sv (Curry et al. 2014).

c. *Gridded hydrographic datasets*

Monthly temperature and salinity fields during August 2014–August 2019 from three observation-based datasets are used. The first dataset is the Multiobservation Global Ocean ARMOR3D Level-4 dataset (Guinehut et al. 2012; Mulet et al. 2012). In the top 1500 m, gridded temperature and salinity are obtained from a combination of synthetic profiles, derived from a vertical projection of satellite data via a multiple linear regression method, and in situ measurements through optimal interpolation. The in situ measurements include profiles from Argo profiling floats, XBT, CTD, and mooring measurements. The property fields below 1500 m are based on *World Ocean Atlas 2018* seasonal climatology. We use the multiyear reprocessed monthly temperature and salinity. The dataset has a horizontal grid of 1/4° and 50 depth levels from 0 to 5500 m.

The second dataset used is the In Situ Analysis System (ISAS) (Nicolas et al. 2021), which is based on measurements from Argo, Deep Argo, and other types of in situ measurements. The optimal interpolation method is applied to obtain the gridded product. The version used in this study is ISAS17, which has 187 standard depth levels from 0 to 5500 m and a horizontal grid of 0.5°. We use delayed mode monthly time series from August 2014 to December 2017 (Gaillard et al. 2016). For the months from January 2018 to August 2019, we use ISAS20_ARGO, which has the same vertical and horizontal resolutions, but only incorporate Argo and Deep Argo data in the gridded fields.

TABLE 1. Density layers and water masses defined in this study. The upper, intermediate, and overflow layers are defined in terms of mean potential density $\overline{\sigma_\theta}$. Water masses contained in each density layer are specified with limits in mean salinity $\overline{S}$.

	Upper layer		Intermediate layer		Overflow layer
$\overline{\sigma_\theta}$(kg m^{-3})	27–27.7		27.7–27.8		>27.8
	ULW	IW	LSW	IW	OW
$\overline{S}$	<34.9	≥34.9	<34.9	≥34.9	≥34.9

Finally, we use the objective analysis product of EN4 from the Met Office Hadley Center (Good et al. 2013). The product incorporates data from the World Ocean Database 13, Global Temperature and Salinity Profile Project, Argo profiling floats, and additional Arctic data. Here, we use monthly time series from version EN4.2.2 with Gouretski and Reseghetti (2010) corrections. The dataset has a horizontal grid of 1° and 42 depth levels from 5 to 5350 m.

d. *Atmospheric reanalysis products*

Monthly air–sea heat and freshwater fluxes of three atmospheric reanalysis products are used to estimate the surface-forced water mass transformation over the Labrador Sea: the National Centers for Environmental Prediction (NCEP)/National Center for Atmospheric Research (NCAR) product (~1.8°; Kalnay et al. 1996), the fifth major global reanalysis produced by ECMWF (ERA5; 30 km; Poli et al. 2016), and the Japanese 55-yr Reanalysis (JRA-55; 1.25°; Ebita et al. 2011). The heat fluxes include the net longwave and shortwave radiation fluxes and the latent and sensible heat fluxes. The freshwater fluxes include evaporation and precipitation. All these fluxes span the time period of August 2014–August 2019.

e. *Water mass definitions*

In this study, layers are defined between isopycnals where the mean diapycnal transformation reaches a local maximum/minimum (Fig. 4a). The water mass contained in each density layer is specified by its characteristic properties at the OSNAP West section (Table 1). Specifically, we define the upper layer as the density layer between 27 and 27.7 kg m^{-3}, where waters are generally warm and highly stratified (Fig. 2). This layer contains both relatively freshwater ($\overline{S} < 34.9$) in the basin interior and along the Labrador coast, which is referred to as the upper-layer water (ULW), and the relatively salty IW ($\overline{S} \geq 34.9$) along the boundary west of Greenland.

The intermediate layer is defined as the density layer between 27.7 and 27.8 kg m^{-3}. In the basin interior and near the Labrador coast, this intermediate layer is filled with LSW, which is characterized by the lowest potential vorticity ($\leq 6 \times 10^{-12}$ m^{-1} s^{-1}) and relatively low salinity ($\overline{S} < 34.9$). Saltier IW ($\overline{S} \geq 34.9$) is also present in the intermediate layer west of Greenland. Underlying the intermediate layer is the overflow layer, whose density is greater than 27.8 kg m^{-3} and salinity is greater than 34.9. This layer contains overflow waters (OW) from the Nordic seas that enter the basin via both the deep boundary current (McCartney 1992; Xu et al. 2015; Pacini et al. 2020; Lozier et al. 2022) and interior pathways (McCartney 1992; Zou et al. 2020b; Lozier et al. 2022). The water mass definitions in this study are overall consistent with those in Pacini et al. (2020).

f. Volume budget for transformation in σ_θ coordinate

The water mass transformation framework was introduced by Walin (1982) and has been widely applied thereafter (e.g., Speer and Tziperman 1992; Speer et al. 1995; Brambilla et al. 2008; Myers and Donnelly 2008; Badin et al. 2010; Petit et al. 2020). Following these previous studies, we evaluate the transformation with respect to σ_θ coordinate. The method is briefly summarized below.

Consider a volume element between ocean surface and a surface of constant σ_θ. The conservation of its volume within a fixed domain is expressed as

$$\frac{\partial V_\sigma}{\partial t} = M_\sigma - G_\sigma, \tag{1}$$

where $\partial V_\sigma/\partial t$ is the temporal volume change (Sv) and M_σ on the rhs of Eq. (1) is the advective transport convergence through the open boundaries, with a positive M_σ leading to an increase of V_σ. Here, we focus on the Labrador Basin, which is bounded by the OSNAP West line to the south, the Davis Strait to the north, and the Hudson Strait to the west (Fig. 1). Since the net flow through the Hudson Strait is small (~0.1 Sv; Drinkwater 1988; Dukhovskoy et al. 2021; Ridenour et al. 2021) and primarily contains very fresh (<34) and light waters (<27 kg m^{-3}; Ridenour et al. 2021), it does not significantly contribute to M_σ over the density range discussed in this study (>27 kg m^{-3}). The parameter M_σ is therefore approximated as

$$M_\sigma = \psi_\sigma|_{\mathrm{OSNAP}} - \psi_\sigma|_{\mathrm{DAVIS}}, \tag{2}$$

where ψ_σ is the overturning streamfunction along a section and is calculated as

$$\psi_\sigma = \int_{\sigma_{\min}}^{\sigma}\int_{x_w}^{x_e} v_\sigma dx d\sigma^*. \tag{3}$$

Here, v_σ is the transport component per unit length per unit density and is perpendicular to the section [m^3 s^{-1} m^{-1} (kg m^{-3})$^{-1}$]. A positive v_σ indicates an overall northwestward flow. The x_w (x_e) for the inner integral denotes the westernmost (easternmost) position of the section. The lower limit of the outer integral $\sigma_{\min}$ is set to be 20 kg m^{-3}. The term σ^* is a dummy variable of the integration. As shown in Fig. S2, the profile of M_σ is primarily determined by $\psi_\sigma|_{\mathrm{OSNAP}}$, with $\psi_\sigma|_{\mathrm{DAVIS}}$ contributing as a net southward throughflow of −1.6 Sv.

The term G_σ on the rhs of Eq. (1) represents the diapycnal volume flux or diapycnal transformation rate taking place in the domain. A positive G_σ indicates a light-to-dense transformation across the σ_θ surface, leading to a decrease of V_σ. The G_σ is estimated as the difference between M_σ and $\partial V_\sigma/\partial t$ and can be further decomposed into a surface-induced term and a residual term, i.e.,

$$G_\sigma = G_\sigma^{\mathrm{sfc}} + G_\sigma^{\mathrm{res}}, \tag{4}$$

where G_σ^{sfc} represents the diapycnal transformation driven by surface density flux acting on outcropping isopycnal σ_θ, which is calculated as

$$G_\sigma^{\mathrm{sfc}} = \frac{1}{\Delta\sigma}\int\int\left[-\frac{\alpha}{C_p}Q + \beta\frac{S}{1-S}(E-P)\right]\Pi_\sigma dx dy, \tag{5}$$

$$\Pi_\sigma = \begin{cases} 1, & |\sigma^* - \sigma| \leq \Delta\sigma/2 \\ 0, & \text{elsewhere} \end{cases},$$

where α (K^{-1}) and C_p (J kg^{-1} K^{-1}) are the thermal expansion coefficient and heat capacity for seawater, respectively; Q (W m^{-2}) represents the net surface heat flux from the atmosphere to the ocean; $E - P$ is evaporation minus precipitation rate (m s^{-1}); S is the sea surface salinity; β is the haline contraction coefficient; and Π_σ identifies the surface areas associated with outcropping isopycnal within a density bin of $\Delta\sigma$, over which the density flux is integrated. In this study, we set $\Delta\sigma$ as 0.1 kg m^{-3}, following previous studies (Speer and Tziperman 1992; Petit et al. 2020). While using smaller bins provides finer resolution of the transformation profile, interpolation of the oceanic and atmospheric datasets to finer scales will introduce unwanted interpolation errors.

The residual term G_σ^{res} in Eq. (4) is estimated as the difference between G_σ and G_σ^{sfc}. It represents diapycnal transformation induced by interior diapycnal mixing and other unresolved processes, such as subsurface penetration of shortwave radiation (Iudicone et al. 2008; Xu et al. 2018), additional mass flux at the domain boundaries (Groeskamp et al. 2019), cabbeling, and thermobaricity due to the nonlinearity of the equation of state (McDougall 1987; Klocker and McDougall 2010; Groeskamp et al. 2016). These latter terms are less important compared to diapycnal mixing in the subpolar North Atlantic according to previous studies (Groeskamp et al. 2016; Xu et al. 2018). In this study, we primarily attribute G_σ^{res} to diapycnal mixing while keeping in mind the potential influence from the other processes.

g. Volume budget for formation in σ_θ coordinate

To evaluate the water mass formation (WMF) rate, we consider volume budget for a specific density layer bounded by σ_θ and $\sigma_\theta + \Delta\sigma$, i.e.,

$$\frac{\partial V_{\Delta\sigma}}{\partial t} = M_{\Delta\sigma} + G_{\Delta\sigma}, \tag{6}$$

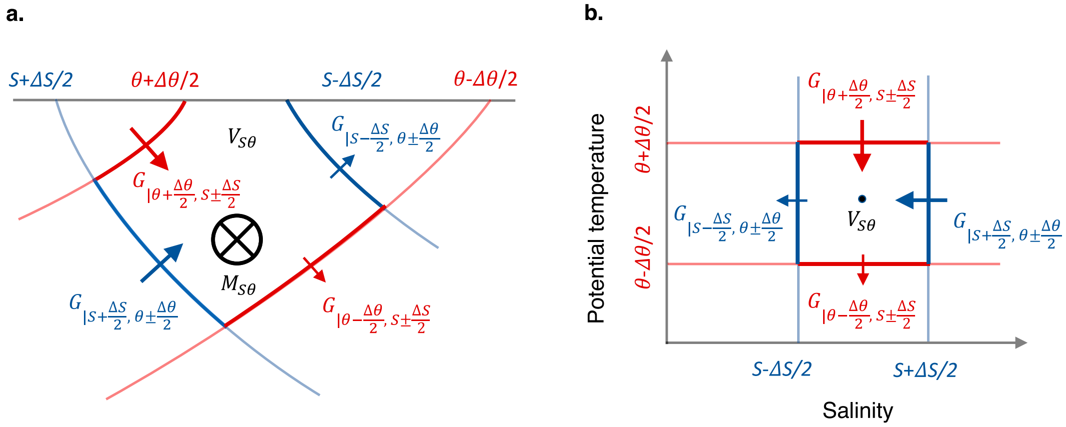

FIG. 3. (a) Schematic of a volume element $V_{S\theta}$ bounded by isohalines $S \pm \Delta S/2$ and isotherms $\theta \pm \Delta\theta/2$. The $M_{S\theta}$ represents advective volume flux through the open boundaries. The $G_{|S,\theta\pm\Delta\theta/2}$ denotes salty-to-fresh transformation across S surface between $\theta \pm \Delta\theta/2$ surfaces. If $G_{|S,\theta\pm\Delta\theta/2}$ increases toward higher salinity, i.e., $G_{|S+\Delta S/2,\theta\pm\Delta\theta/2} > G_{|S-\Delta S/2,\theta\pm\Delta\theta/2}$, there is a diahaline volume flux convergence, which leads to a net thermohaline formation. Similar cases apply to $G_{|\theta,S\pm\Delta S/2}$. (b) The same volume element in thermohaline (S–θ) coordinates. Figures are adapted from Groeskamp et al. (2014a) and Mackay et al. (2018).

where $\partial V_{\Delta\sigma}/\partial t$ denotes the volume change of the layer, $M_{\Delta\sigma}$ denotes advective convergence through the open boundaries, and $G_{\Delta\sigma}$ represents the convergence of diapycnal volume flux between σ_θ and $\sigma_\theta + \Delta\sigma$ and is defined as the water mass formation rate of the layer,

$$G_{\Delta\sigma} = -\Delta\sigma\frac{\partial G_\sigma}{\partial\sigma}. \tag{7}$$

The total formation rate $G_{\Delta\sigma}$ can be further attributed to either surface forcing or interior mixing,

$$G_{\Delta\sigma} = G^{\mathrm{sfc}}_{\Delta\sigma} + G^{\mathrm{res}}_{\Delta\sigma}. \tag{8}$$

h. Volume budget in S–θ coordinates

We follow Mackay et al. (2018, 2020) for the construction of volume budget in thermohaline (S–θ) coordinates. In their study, the thermohaline formation rate was estimated using a regional thermohaline inverse method, which was originally based on a global thermohaline inverse method developed by Groeskamp et al. (2014a). Here, the thermohaline formation rate is directly estimated from observational and atmospheric reanalysis datasets.

Consider a volume element $V_{S\theta}$ that is bounded by isohalines $S \pm \Delta S/2$ and isotherms $\theta \pm \Delta\theta/2$ (Fig. 3). Its temporal evolution is governed by

$$\frac{\partial V_{S\theta}}{\partial t} = M_{S\theta} + \boldsymbol{\nabla}_{S\theta}\cdot\mathbf{G}_{S\theta}, \tag{9}$$

where $M_{S\theta}$ denotes advective transport convergence between OSNAP West and the Davis Strait, i.e.,

$$M_{S\theta} = \psi_{S\theta}|_{\mathrm{OSNAP}} - \psi_{S\theta}|_{\mathrm{Davis}}, \tag{10}$$

where

$$\psi_{S\theta} = \int\!\!\int \Pi_S\Pi_\theta v\,dxdz, \tag{11}$$

in which v is the velocity component (m s^{-1}) perpendicular to the section. Discrete functions Π_S and Π_θ are defined to identify grid points along the section where salinities and temperatures are within the $S \pm \Delta S/2$ and $\theta \pm \Delta\theta/2$ ranges. In this study, ΔS is set as 0.1 and $\Delta\theta$ is set as 1°C.

The $\mathbf{G}_{S\theta}$ in Eq. (9) represents the diathermohaline volume flux, and $\mathbf{G}_{S\theta} = (G_{|S,\theta\pm\Delta\theta/2}, G_{|\theta,S\pm\Delta S/2})$ (Mackay et al. 2018). Here, positive $G_{|S,\theta\pm\Delta\theta/2}$ denotes salty-to-fresh transformation across S surface between $\theta \pm \Delta\theta/2$ surfaces, and positive $G_{|\theta,S\pm\Delta S/2}$ denotes warm-to-cold transformation across θ surface between $S \pm \Delta S/2$ surfaces (Fig. 3). The gradient operator is defined as $\boldsymbol{\nabla}_{S\theta} = (\partial/\partial S, \partial/\partial\theta)$, and $\boldsymbol{\nabla}_{S\theta}\cdot\mathbf{G}_{S\theta} = (\partial G_{|S,\theta\pm\Delta\theta/2}/\partial S, \partial G_{|\theta,S\pm\Delta S/2}/\partial\theta)$ is the convergence of diathermohaline flux. It represents the thermohaline formation rate between $\theta \pm \Delta\theta/2$ and $S \pm \Delta S/2$ surfaces and is estimated as the difference between $M_{S\theta}$ and $\partial V_{S\theta}/\partial t$.

The term $\boldsymbol{\nabla}_{S\theta}\cdot\mathbf{G}_{S\theta}$ can be further decomposed into

$$\boldsymbol{\nabla}_{S\theta}\cdot\mathbf{G}_{S\theta} = \boldsymbol{\nabla}_{S\theta}\cdot\mathbf{G}^{\mathrm{sfc}}_{S\theta} + \boldsymbol{\nabla}_{S\theta}\cdot\mathbf{G}^{\mathrm{res}}_{S\theta}, \tag{12}$$

where $\boldsymbol{\nabla}_{S\theta}\cdot\mathbf{G}^{\mathrm{sfc}}_{S\theta}$ represents the thermohaline formation rate induced by surface heat and freshwater fluxes, which is calculated as

$$\begin{aligned}\boldsymbol{\nabla}_{S\theta}\cdot\mathbf{G}^{\mathrm{sfc}}_{S\theta} = \frac{\partial}{\partial S}\left[\int\!\!\int -(E-P)S\Pi_\theta\Pi_S dxdy\right] \\ + \frac{\partial}{\partial\theta}\left[\int\!\!\int -\frac{Q}{\rho C_p}\Pi_\theta\Pi_S dxdy\right],\end{aligned} \tag{13}$$

where $\Pi_\theta\Pi_S$ is defined to identify surface areas with outcropping isotherm θ and outcropping isohaline S within bins of $\Delta\theta$ and ΔS and $\boldsymbol{\nabla}_{S\theta}\cdot\mathbf{G}^{\mathrm{res}}_{S\theta}$ represents the formation rate induced by interior mixing and other unresolved processes that might cause $V_{S\theta}$ to change. As suggested by Mackay et al. (2018, 2020), interior mixing dominates $\nabla_{S\theta}\cdot\mathbf{G}^{\rm res}_{S\theta}$ in the subpolar North Atlantic. We estimate this term as a residual of the other terms given by Eq. (12).

If Eq. (9) is integrated across all isohalines (isotherms), we obtain the volume budget for the formation within the thermal layer between $\theta \pm \Delta\theta/2$ (haline layer between $S \pm \Delta S/2$),

$$\frac{\partial V_{\Delta\theta}}{\partial t} = M_{\Delta\theta} + G_{\Delta\theta} = M_{\Delta\theta} + (G^{\rm sfc}_{\Delta\theta} + G^{\rm res}_{\Delta\theta}), \tag{14}$$

$$\frac{\partial V_{\Delta S}}{\partial t} = M_{\Delta S} + G_{\Delta S} = M_{\Delta S} + (G^{\rm sfc}_{\Delta S} + G^{\rm res}_{\Delta S}),$$

where $G_{\Delta\theta}$ ($G_{\Delta S}$) represents the formation rate in that thermal (haline) layer. By further integrating Eq. (14) from maximum temperature (salinity) to a certain isotherm θ (isohaline S), we obtain the volume budget for diathermal (diahaline) transformation,

$$\frac{\partial V_{\theta}}{\partial t} = M_{\theta} - G_{\theta} = M_{\theta} - (G^{\rm sfc}_{\theta} + G^{\rm res}_{\theta}), \tag{15}$$

$$\frac{\partial V_{S}}{\partial t} = M_{S} - G_{S} = M_{S} - (G^{\rm sfc}_{S} + G^{\rm res}_{S}).$$

A positive G_θ (G_S) represents a warm-to-cold (salty-to-fresh) transformation and note that

$$G_\theta = -\frac{1}{\Delta\theta}\int_{\theta_{\rm max}}^{\theta} G_{\Delta\theta}\,d\theta^* = -\frac{1}{\Delta\theta\Delta S}\int_{\theta_{\rm max}}^{\theta}\int_{S_{\rm max}}^{S_{\rm min}} \nabla_{S\theta}\cdot\mathbf{G}_{S\theta}\,dS^*\,d\theta^*, \tag{16}$$

$$G_S = -\frac{1}{\Delta S}\int_{S_{\rm max}}^{S} G_{\Delta S}\,dS^* = -\frac{1}{\Delta\theta\Delta S}\int_{S_{\rm max}}^{S}\int_{\theta_{\rm max}}^{\theta_{\rm min}} \nabla_{S\theta}\cdot\mathbf{G}_{S\theta}\,d\theta^*\,dS^*.$$

i. The mean and uncertainty estimates

To derive the mean transformation rate $\overline{G}_\gamma$ (γ being σ, θ, or S) and its uncertainty, we first calculate the mean volume change $\overline{\partial V_\gamma/\partial t}$ and its uncertainty. In each month during August 2014–August 2019, $\partial V_\gamma/\partial t$ is calculated with each of the three oceanic datasets (ARMOR3D, ISAS, and EN4). The average among datasets is recorded as $(\partial V_\gamma/\partial t)^m$, where m denotes the number of months ($m = 1, 2, \ldots, 61$), and the standard deviation among datasets is STD^m. To derive the 61-month mean volume change $\overline{\partial V_\gamma/\partial t}$ and its uncertainty, we use a Monte Carlo approach. Specifically, for the ith iteration, the volume change in an individual month, i.e., $(\partial V_\gamma/\partial t)^m_i$, is randomly generated from a normal distribution with a mean of $(\partial V_\gamma/\partial t)^m$ and STD^m. This step gives a 61-month volume change time series, from which we draw the mean for this iteration $(\overline{\partial V_\gamma/\partial t})_i$. The above steps are repeated for $N = 5000$ times, and the mean volume change can be estimated as

$$\overline{\frac{\partial V_\gamma}{\partial t}} = \frac{1}{N}\sum_{i=1}^{N}\left(\overline{\frac{\partial V_\gamma}{\partial t}}\right)_i. \tag{17}$$

The standard error (SE) associated with $\overline{\partial V_\gamma/\partial t}$ is given by

$${\rm SE}_V = \sqrt{\frac{1}{N-1}\sum_{i=1}^{N}\left[\left(\overline{\frac{\partial V_\gamma}{\partial t}}\right)_i - \overline{\frac{\partial V_\gamma}{\partial t}}\right]^2}. \tag{18}$$

Next, we calculate the mean advective volume flux through the open boundaries. At both OSNAP West and the Davis Strait, monthly ψ_γ is calculated using gridded observational data and is then averaged temporally to obtain $\overline{\psi}_\gamma$. The SE is estimated from the monthly STD and degrees of freedom (DOF),

$${\rm SE}_\psi = \frac{\rm STD}{\sqrt{\rm DOF}}. \tag{19}$$

The mean transport convergence $\overline{M}_\gamma$ between the two sections and its SE are therefore

$$\overline{M}_\gamma = \overline{\psi}_{\gamma,{\rm OSNAP}} - \overline{\psi}_{\gamma,{\rm DAVIS}}, \tag{20}$$

$${\rm SE}_M = \sqrt{{\rm SE}^2_{\psi,{\rm OSNAP}} + {\rm SE}^2_{\psi,{\rm DAVIS}}}. \tag{21}$$

With $\overline{M}_\gamma$ and $\overline{\partial V_\gamma/\partial t}$, the mean transformation rate $\overline{G}_\gamma$ is estimated as the difference between the two following Eq. (1). The associated SE is estimated as the square root of the sum of SE for $\overline{M}_\gamma$ and SE for $\overline{\partial V_\gamma/\partial t}$, similar to that in Eq. (21).

The monthly transformation rate induced by surface flux ($G^{\rm sfc}_\gamma$) is calculated by combining the three atmospheric reanalysis products, NCEP/NCAR, ERA5, and JRA-55, with the three oceanic datasets EN4, ARMOR3D, and ISAS. Before calculating, all datasets are subsampled onto the ERA5 horizontal grid of 30 km. We apply one of the atmospheric datasets (e.g., ERA5) on the outcropping area determined by one of the oceanic datasets (e.g., ARMOR3D) to derive monthly $G^{\rm sfc}_\gamma$. The nine individual estimations of $G^{\rm sfc}_\gamma$ are then averaged to obtain $(G^{\rm sfc}_\gamma)^m$ and STD^m, with m denoting the number of months. The 61-month mean $\overline{G^{\rm sfc}_\gamma}$ and its uncertainty are estimated in a similar way to those for $\overline{\partial V_\gamma/\partial t}$ using a Monte Carlo approach. The mean transformation induced by the unresolved processes $\overline{G^{\rm res}_\gamma}$ is estimated as the difference between the total ($\overline{G}_\gamma$) and the surface-induced transformation ($\overline{G^{\rm sfc}_\gamma}$). Its SE is estimated as the square root of the sum of SE for $\overline{G}_\gamma$ and SE for $\overline{G^{\rm sfc}_\gamma}$, similar to that in Eq. (21).

Finally, the mean formation rate $\overline{G}_{\Delta\gamma}$ is calculated as the difference of mean transformation rates between the two bounding isosurfaces γ and $\gamma + \Delta\gamma$. Its uncertainty is estimated as the square root of the sum of SE associated with the two transformation rates, similar to that in Eq. (21). Unless otherwise noted, the reported estimates represent the time-mean plus/minus uncertainty in the mean.

3. Results in σ_θ coordinate

a. Mean transformation

The volume budget associated with the mean water mass transformation in σ_θ space during August 2014–August 2019 is shown in Fig. 4a. The mean volume change ($\overline{\partial V_\sigma/\partial t}$) at each isopycnal is smaller than 0.1 Sv, meaning that a quasi-steady

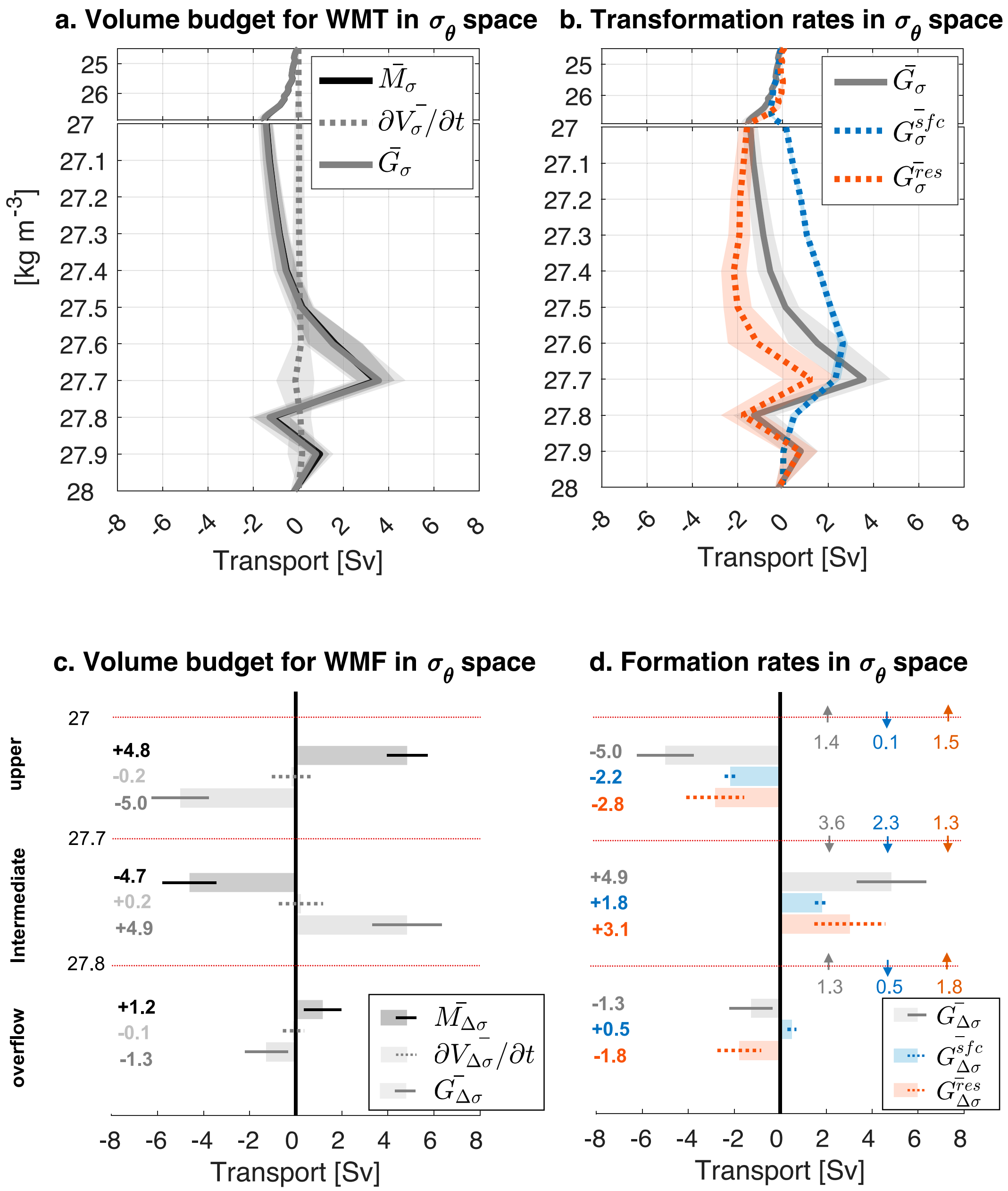

FIG. 4. (a) Volume budget for WMT in σ_θ space following Eq. (1). Advective transport convergence between OSNAP West and the Davis Strait $\overline{M_\sigma}$ is plotted in solid black. The mean volume change $(\overline{\partial V_\sigma/\partial t})$ is shown as a gray dotted line, and the mean diapycnal transformation $(\overline{G_\sigma})$ is plotted in solid gray. Positive $\overline{G_\sigma}$ represents a light-to-dense transformation. Shading represents SE. (b) Transformation rates, including the total $\overline{G_\sigma}$ (solid gray), the surface-induced component $\overline{G_\sigma^{\rm sfc}}$ (dotted blue), and the residual term $\overline{G_\sigma^{\rm res}}$ (dotted orange). (c) Volume budget for WMF following Eq. (6). $\overline{M_{\Delta\sigma}}$, $\overline{\partial V_{\Delta\sigma}/\partial t}$, and $\overline{G_{\Delta\sigma}}$ in each density layer are shown as gray bars and are also labeled to the left. The associated SEs are indicated with sticks. Horizontal red dotted lines correspond to isopycnals of 27, 27.7, and 27.8 kg m^{-3} that delimit the three density layers (Table 1). (d) Formation rates and their SEs, including the total $\overline{G_{\Delta\sigma}}$ (gray), the surface-induced component $\overline{G_{\Delta\sigma}^{\rm sfc}}$ (blue), and the residual term $\overline{G_{\Delta\sigma}^{\rm res}}$ (orange). The mean formation rates in each density layer are labeled to the left, with positive (negative) signs indicating water mass formations (destructions). The absolute transformation rates across the bounding isopycnals for each layer are also labeled, with the transformation directions indicated as arrows.

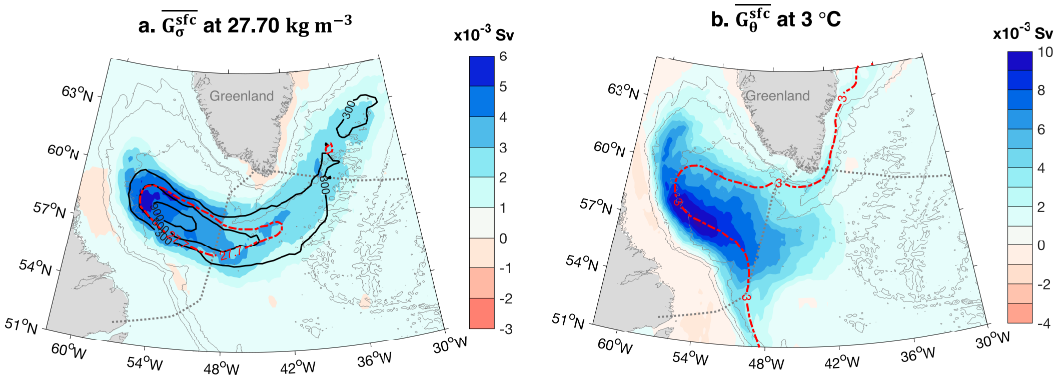

FIG. 5. (a) Spatial distribution of $\overline{G^{sfc}_{\sigma}}$ at 27.7 kg m^{-3} during August 2014–August 2019. Black contours represent winter mixed layer depths (same as those in Fig. 1). The red dashed contour denotes outcropping isopycnal of 27.7 kg m^{-3} in winter months. (b) Spatial distribution of $\overline{G^{sfc}_{\theta}}$ at 3°C during the same time period. Red dashed contour denotes outcropping isotherm of 3°C in winter months.

state is reached and that the mean advective convergence between OSNAP West and the Davis Strait ($\overline{M_{\sigma}}$) is balanced by the mean diapycnal transformation $\overline{G_{\sigma}}$ at each isopycnal.

At densities less than 27 kg m^{-3}, $\overline{M_{\sigma}}$ is a transport divergence, which is attributed to a larger export of the lightest waters along the Labrador shelf compared to their import along the Greenland shelf (Fig. 2d). The dense-to-light transformation that balances this transport divergence is likely due to freshwater input from the surface and lateral boundaries, sea ice melt, and/or mixing processes. These waters are not the focus of our study and will not be discussed further. Here, we focus on transformation taking place in the basin interior where σ_{θ} is overall greater than 27 kg m^{-3}.

The strongest transformation in the basin interior occurs at 27.7 kg m^{-3}, where $\overline{G_{\sigma}}$ is 3.6 ± 1.2 Sv and corresponds to a light-to-dense volume flux (Fig. 4a). To explore the driving mechanisms for $\overline{G_{\sigma}}$, we decompose it into a component induced by surface buoyancy flux $\overline{G^{sfc}_{\sigma}}$ and a residual term $\overline{G^{res}_{\sigma}}$ that is primarily attributed to mixing. As shown in Fig. 4b, $\overline{G^{sfc}_{\sigma}}$ is positive at each isopycnal greater than 27 kg m^{-3}, suggesting a consistent light-to-dense transformation in response to buoyancy loss at the ocean surface. At 27.7 kg m^{-3}, $\overline{G^{sfc}_{\sigma}}$ is 2.3 ± 0.2 Sv, which accounts for 64% of $\overline{G_{\sigma}}$ at the same isopycnal. The $\overline{G^{sfc}_{\sigma}}$ estimated in this study is higher than, but still comparable to, that in a previous study by Petit et al. (2020), who reported a surface-induced transformation of 1.5 ± 0.7 Sv during August 2014–May 2016. The spatial distribution of $\overline{G^{sfc}_{\sigma}}$ reveals its maximum in the central-western Labrador Basin, where winter mixed layers are deep and 27.7 kg m^{-3} outcrops (Fig. 5a). Outside of the Labrador Basin, relatively high $\overline{G^{sfc}_{\sigma}}$ at 27.7 kg m^{-3} extends northeastward into the central-western Irminger Sea, another site with frequent convective events (Pickart et al. 2003; de Jong et al. 2012, 2018). This widespread surface-induced transformation in the Labrador and Irminger Basins is consistent with previous studies—using Argo float data (Piron et al. 2017) and an eddy-rich ocean/sea ice model (Rühs et al. 2021)—that have noted extended deep convection in these basins after 2015. Piron et al. (2017) further attributed the extended deep convection to exceptional surface heat loss and strong wind event occurrences during winters in these years.

The remaining 36% of the light-to-dense transformation at 27.7 kg m^{-3} is accomplished by $\overline{G^{res}_{\sigma}}$, which is 1.3 ± 1.2 Sv. Diapycnal mixing associated with deepening mixed layers has been shown to drive light-to-dense transformation in the Labrador Sea, according to both high-resolution ocean circulation models (Xu et al. 2018) and idealized simulations (Brüggemann and Katsman 2019). In particular, Xu et al. (2018) investigated the spatial distribution of mixing-induced diapycnal transformation using a 1/12° model HYCOM and found that at isopycnal $\sigma_2 = 36.815$ kg m^{-3} (potential density referenced to 2000 dbar), corresponding to $\sigma_{\theta} \approx 27.72$ kg m^{-3}, the light-to-dense transformation primarily took place around and within the convection site. Surrounding the light-to-dense transformation, mixing also induced a dense-to-light transformation at the same isopycnal, which was attributed to mesoscale eddies acting on the winter mixed layer base (Xu et al. 2018). This eddy-induced restratification during and after convection has previously been revealed by extra-high-resolution ocean models—1/60° NEMO (Pennelly and Myers 2020) and 1-km ROMS (Tagklis et al. 2020), which show important upward and horizontal eddy buoyancy flux that counteracts the deepening of the mixed layer (Tagklis et al. 2020; Li et al. 2023). We will return to this point in section 4.

At isopycnals greater than 27.8 kg m^{-3}, outcroppings at the sea surface occur less frequently, and $\overline{G_{\sigma}}$ is primarily accomplished by $\overline{G^{res}_{\sigma}}$. Specifically, at 27.8 kg m^{-3} which delimits the overflow layer from the intermediate layer (Table 1), dense-to-light transformation takes place ($\overline{G_{\sigma}} = -1.3 \pm 0.9$ Sv) due to mixing ($\overline{G^{res}_{\sigma}} = -1.8 \pm 1.0$ Sv). This mixing-induced deep upwelling may be explained by the bottom boundary layer theory (Ferrari et al. 2016; de Lavergne et al. 2016), which argues that turbulent buoyancy flux converges in the bottom boundary layer and therefore results in deep-water upwelling. Since the bottom boundary layer is only a few tens of meters thick, the diapycnal rising at 27.8 kg m^{-3} is therefore confined to a very thin layer of a narrow annulus along the sloping topography of the basin (Ferrari et al. 2016). At 27.9 kg m^{-3}, diapycnal transformation is weak and is associated with relatively large uncertainty ($\overline{G_\sigma} = 0.7 \pm 0.8$), precluding a robust conclusion. Further study is needed to understand these deep diapycnal motions in the Labrador Sea.

b. Mean formation

The convergence (divergence) of transformation between isopycnals gives the water mass formation (destruction) rate. Here, we discuss the mean formation rates in three density layers defined in Table 1. In the upper layer (27–27.7 kg m^{-3}), there is net destruction over the 5-yr time period, with $\overline{G_{\Delta\sigma}} = -5.0 \pm 1.2$ Sv (Fig. 4c). The destruction is due to the transformation divergence between the two bounding isopycnals: a dense-to-light transformation of 1.4 Sv at 27 kg m^{-3} and a light-to-dense transformation of 3.6 Sv at 27.7 kg m^{-3} (Fig. 4d). This transformation divergence is nearly equally contributed by interior mixing ($\overline{G_{\Delta\sigma}^{\rm res}} = -2.8 \pm 1.3$ Sv) and surface forcing ($\overline{G_{\Delta\sigma}^{\rm sfc}} = -2.2 \pm 0.2$ Sv).

In the intermediate layer (27.7–27.8 kg m^{-3}), a transformation convergence is induced by a light-to-dense transformation of 3.6 Sv at 27.7 kg m^{-3} and a dense-to-light transformation of 1.3 Sv at 27.8 kg m^{-3}, resulting in a formation rate of 4.9 ± 1.5 Sv in this layer. Importantly, 63% of the transformation convergence is induced by mixing ($\overline{G_{\Delta\sigma}^{\rm res}} = 3.1 \pm 1.5$ Sv), which converts waters both lighter than 27.7 kg m^{-3} (1.3 Sv) and denser than 27.8 kg m^{-3} (1.8 Sv) into the intermediate layer. That is to say, both the upper-layer waters and the deeper overflow waters are converted into the intermediate layer by mixing. By comparison, surface forcing is responsible for a smaller portion (37%) of the formation rate ($\overline{G_{\Delta\sigma}^{\rm sfc}} = 1.8 \pm 0.3$ Sv). These results highlight the importance of diapycnal mixing for water mass formation in the intermediate layer, which primarily contains LSW. Finally, in the overflow layer (>27.8 kg m^{-3}), there is a destruction ($\overline{G_{\Delta\sigma}} = -1.3 \pm 0.9$ Sv) that is primarily induced by mixing ($\overline{G_{\Delta\sigma}^{\rm res}} = -1.8 \pm 1.0$ Sv). Surface forcing, on the other hand, is responsible for producing only 0.5 ± 0.2 Sv in this layer.

To summarize, in section 3, we have estimated the mean transformation and formation rates with respect to σ_θ space in the Labrador Basin during August 2014–August 2019. The maximum light-to-dense transformation rate is 3.6 ± 1.2 Sv and is achieved at 27.7 kg m^{-3}. Both surface buoyancy loss and interior mixing are important in driving the transformation, with a stronger contribution from the former (64%) than the latter (36%). Convergence of transformations in the LSW density layer 27.7–27.8 kg m^{-3} leads to a production rate of 4.9 ± 1.5 Sv, 63% of which (3.1 ± 1.5 Sv) is accomplished by interior mixing, with the remaining 37% (1.8 ± 0.3 Sv) attributed to surface buoyancy forcing. These results underscore the importance of mixing on the diapycnal transformation and formation associated with the LSW layer.

4. Results in S–θ coordinates

a. Mean thermohaline formation

To further understand the physical processes driving the thermal and haline anomalies in the Labrador Sea, we evaluate the water mass formation rates with respect to the thermohaline (S–θ) coordinates. The mean thermohaline formation rate ($\overline{\boldsymbol{\nabla}_{S\theta} \cdot \mathbf{G}_{S\theta}}$) over the 5-yr time period is shown in Fig. 6a. The prominent feature is a destruction of the warmer, saltier waters and a formation of the colder, fresher waters in the upper–intermediate layers (<27.80 kg m^{-3}), which suggests significant diathermal and diahaline volume fluxes and is the focus of this section.

More quantitatively, the mean warm-to-cold transformation ($\overline{G_\theta}$) is as large as 10.7 ± 0.5 Sv at 4°C (Fig. 6b; Zou et al. 2020a), which is the primary attribution of the destruction of the warmer waters between 4° and 5°C ($\overline{G_{\Delta\theta}} = -7.6 \pm 1.3$ Sv) and the formation of the colder waters between 3° and 4°C ($\overline{G_{\Delta\theta}} = 9.5 \pm 1.4$ Sv). In salinity space, a strong salty-to-fresh transformation ($\overline{G_S}$) of 10.7 ± 3.4 Sv takes place at 34.9 (Fig. 6c), leading to a destruction of the saltier layer between 34.9 and 35 ($\overline{G_{\Delta S}} = -10.6 \pm 3.4$ Sv) and a production of the fresher layer between 34.8 and 34.9 ($\overline{G_{\Delta S}} = 8.6 \pm 3.5$ Sv). This haline transformation mostly occurs in the upper–intermediate layers but is also contributed partially by the overflow layer. Collectively, the strongest destruction (formation) of the warmer waters of 4°–5°C (colder waters of 3°–4°C) is in concert with the strongest destruction (formation) of the saltier waters of 34.9–35 (fresher waters of 34.8–34.9) in the upper–intermediate layers. As shown in Fig. 6a, these thermohaline volume changes largely occur along constant density surfaces smaller than 27.80 kg m^{-3} but across spiciness surfaces (spiciness measures temperature and salinity changes along a constant density surface), suggesting isopycnal mixing as the primary driving mechanism.

To further understand the physical processes responsible for the abovementioned thermohaline volume changes, we next quantify the contributions from interior mixing and surface flux to the thermohaline formation rates.

b. Mixing-induced thermohaline formation

The mean thermohaline formation rate induced by interior mixing is revealed by $\overline{\boldsymbol{\nabla}_{S\theta} \cdot \mathbf{G}_{S\theta}^{\rm res}}$ (Fig. 7). It is responsible for the strong thermohaline volume changes discussed in section 4a, including the destruction of the saltier and warmer layer within [34.9–35, 4°–5°C] and the formation of the fresher and colder layer within [34.8–34.9, 3°–4°C] (black circles in Figs. 6a and 7a). The mixing-induced thermal and haline anomalies are very likely associated with mesoscale eddies, which can efficiently stir tracers along density surfaces. This is further illustrated by identifying the geographic locations of waters having the above characteristic [S, θ]. As shown in Fig. 8a, based on ARMOR3D, waters with properties of [34.9–35, 4°–5°C] mostly locate to the west of Greenland and in the northern Labrador Basin (blue curves), while waters with properties of [34.8–34.9, 3°–4°C] concentrate in the central basin where convection occurs (red curves). Similar results are found based on ISAS and EN4 (Figs. S3a and S4a). The depth range over which both sets of [S, θ] are present is between 100 and 600 m (not shown). Thus, the associated thermohaline destruction and formation, which imply a diathermohaline transformation from [34.9–35, 4°–5°C] to [34.8–34.9, 3°–4°C], should primarily occur along density

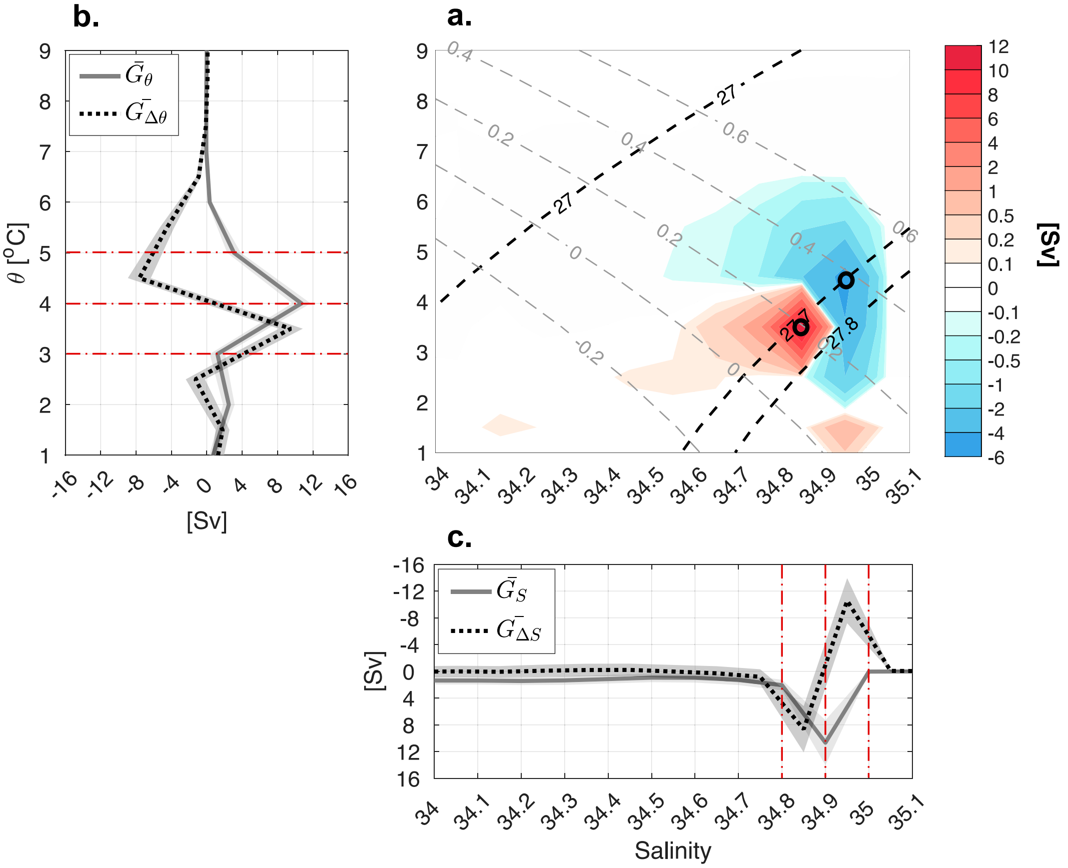

FIG. 6. (a) Mean thermohaline formation rate $\overline{\nabla_{S\theta}\cdot \mathbf{G}_{S\theta}}$. Positive (negative) value denotes formation (destruction) in the corresponding S–θ bin. Black circles denote S–θ bins with the strongest thermohaline volume changes. Reference potential density is contoured in dashed black, and reference spiciness is contoured in dashed gray. (b) Mean diathermal transformation $\overline{G_\theta}$ (solid gray) and formation $\overline{G_{\Delta\theta}}$ (dotted black) rates. Positive $\overline{G_\theta}$ represents a warm-to-cold transformation. Positive $\overline{G_{\Delta\theta}}$ represents convergence of $\overline{G_\theta}$ between isotherms and therefore formation of that thermal layer. Horizontal red dashed lines denote isotherms of 3°, 4°, and 5°C. (c) As in (b), but in S coordinate. Vertical red dashed lines denote isohalines of 34.8, 34.9, and 35.

surfaces in the upper–intermediate layers of the northern Labrador Basin, where the red and blue curves get close or overlap.

Apparently, the saltier and warmer waters of [34.9–35, 4°–5°C] are the IW carried into the Labrador Basin by the West Greenland Current, and the fresher and colder waters of [34.8–34.9, 3°–4°C] are the ULW and LSW in the interior. When the West Greenland Current encounters the steep topography near Cape Desolation, it becomes barotropically and/or baroclinically unstable, generating coherent Irminger Rings (e.g., Eden and Böning 2002; Lilly et al. 2003; Bracco et al. 2008; Rieck et al. 2019; Gou et al. 2023), noncoherent mesoscale (de Jong et al. 2016), and submesoscale features (Tagklis et al. 2020). These submesoscale and mesoscale features are shown to facilitate lateral exchange of heat and salt between the warm, salty boundary and the cold, fresh interior in the northern Labrador Basin (Cuny et al. 2002; Palter et al. 2008; de Jong et al. 2016; Georgiou et al. 2021; Tagklis et al. 2020). Here, we further show, from a quantitative perspective, the importance of lateral exchange along isopycnals, in facilitating water mass transformations in terms of their thermohaline anomalies. This result is consistent with Mackay et al. (2020), who applied the regional thermohaline inverse method on observation-based datasets and found isopycnal mixing as the primary pathway for the newly convected LSW to enter the boundary current.

It is interesting to note in Fig. 7a that mixing also drives thermohaline volume changes at fresher isohalines (<34.7). Specifically, it leads to a formation of warmer waters between 3° and 4°C and a destruction of colder waters between 2° and 3°C (Fig. 7b), with little change in salinity (Fig. 7c). According to a preliminary analysis on the seasonal variability of transformation (not shown), we find that this mixing-induced transformation primarily occurs in the winter months (January–March). To further illustrate the potential process responsible for this cold-to-warm transformation, we locate waters with properties of [34.6–34.7, 3°–4°C] and [34.6–34.7, 2°–3°C] (black diamonds in Fig. 7a). As shown in Fig. 8b, the occurrences of the two sets of [S, θ] based on ARMOR3D overlap along the rim of the convection site in the central basin and

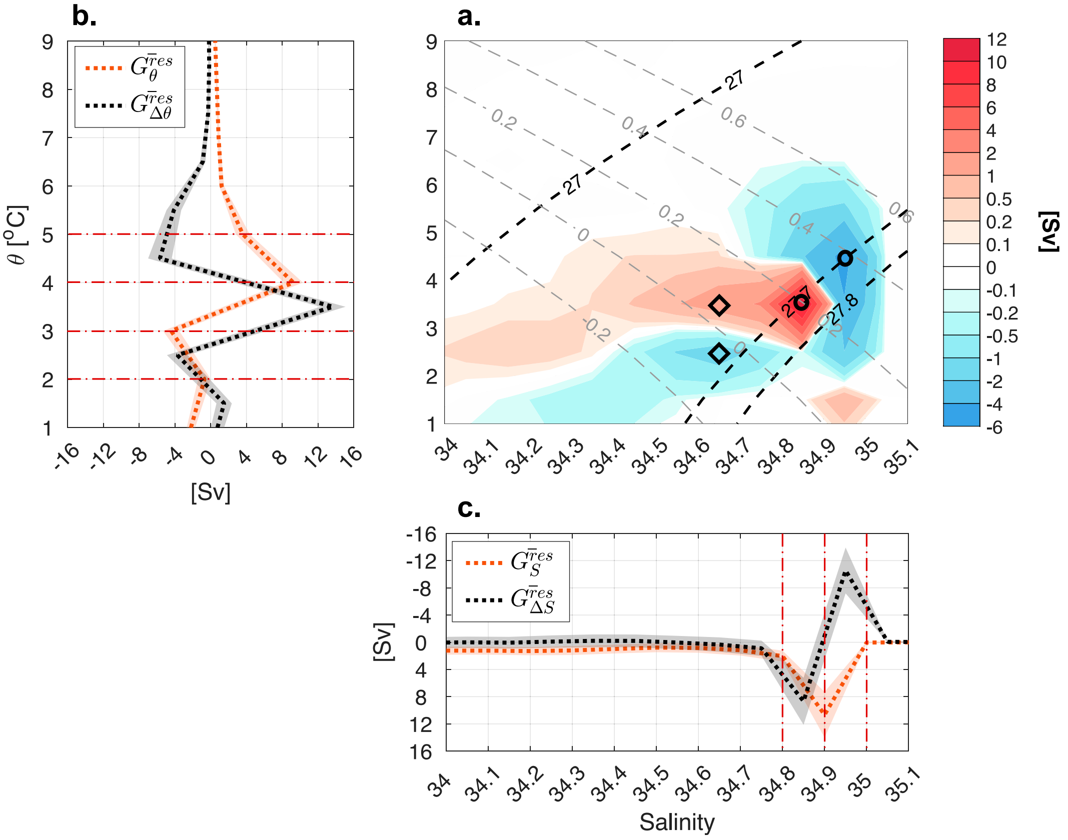

FIG. 7. (a) Mean thermohaline formation rate induced by mixing $\overline{\nabla_{S\theta}\cdot\mathbf{G}_{S\theta}^{\text{res}}}$. Black markers denote S–θ bins with strong volume changes. (b) Mean diathermal transformation $\overline{G_{\theta}^{\text{res}}}$ (dotted orange) and formation $\overline{G_{\Delta\theta}^{\text{res}}}$ (dotted black) due to mixing. Horizontal red dashed lines denote isotherms of 2°, 3°, 4°, and 5°C. (c) As in (b), but in S coordinate. Vertical red dashed lines denote isohalines of 34.8, 34.9, and 35.

along the western boundary. In ISAS and EN4, the overlapping region is more concentrated toward the western boundary of the basin (Figs. S3 and S4). The depth range over which both sets of [S, θ] are present is shallower than 400 m (not shown).

Based on the geographic locations and the fact that the cold-to-warm transformation primarily occurs in winter, we surmise that the mixing is associated with eddies and filaments developed at the sharp front between the wintertime convective patch and the buoyant surrounding waters (Jones and Marshall 1997; Xu et al. 2018). One of the candidates is the convective eddies, which are characterized by cold and fresh anomalies analogous to the newly convected waters (Lilly et al. 2003; Chanut et al. 2008). These eddies have been suggested to be the major driver of rapid stratification after convection in the central Labrador Sea according to a high-resolution ocean circulation model (Rieck et al. 2019). In addition, the unstable Labrador Current has also been shown to generate eddies known as the boundary current eddies (Chanut et al. 2008; Rieck et al. 2019). Both types of eddies, along with other small-scale filaments, may act to restratify the convective interior and result in a cold-to-warm (thus dense-to-light) transformation. Similar dense-to-light transformation along the rim of the convection site is shown in a modeling study by Xu et al. (2018).

By comparing Fig. 7 with Fig. 6, we can see that the volume changes induced by the restratifying eddies are not reflected in the total thermohaline volume changes. This implies that surface forcing acts to drive volume changes opposite to those induced by mixing, which is further illustrated in the next section.

c. *Surface-induced thermohaline formation*

The mean thermohaline volume change induced by surface flux is shown in Fig. 9. Because surface freshwater flux plays a negligible role (Fig. 9c; Petit et al. 2020; Bebieva and Lozier 2023), the surface-induced volume change is primarily driven by surface heat flux, and thus, the transformation occurs in thermal space. Specifically, the strongest warm-to-cold transformation $\overline{G_{\theta}^{\text{sfc}}}$ in response to surface heat loss is 5.6 ± 0.3 Sv at 3°C (Fig. 9b). While the transformation occurs at a cold isotherm, it concentrates at fresher isohalines of 34.6–34.7 (black diamonds in Fig. 9a) and thus at lighter isopycnals (<27.7 kg m^{-3}). The spatial distribution of $\overline{G_{\theta}^{\text{sfc}}}$ shown in Fig. 5b reveals its occurrence in the southwestern Labrador Sea, where the 3°C isotherm outcrops most frequently during

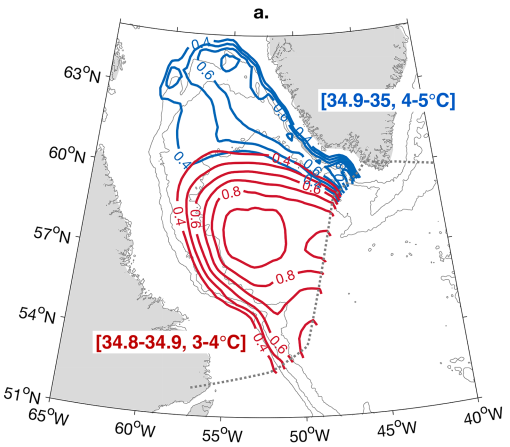

FIG. 8. Normalized number of occurrences within specific [S, θ] ranges during August 2014–August 2019 based on ARMOR3D. Specifically, at each horizontal grid point, we count the number of months when S and θ fall in specified ranges at each vertical level and then integrate across all vertical levels to obtain the total number of occurrences. Plotted is the total number of occurrences normalized by its maximum among all grid points in the basin. (a) Blue curves correspond to the normalized number of occurrences within [34.9–35, 4°–5°C]. Red curves correspond to those within [34.8–34.9, 3°–4°C]. (b) Blue (red) curves correspond to the normalized number of occurrences within [34.6–34.7, 2°–3°C] [34.6–34.7, 3°–4°C]. In both panels, only regions with normalized numbers greater than 0.4 are shown. The plots based on ISAS and EN4 are shown in Figs. S3 and S4.

winters (Fig. S5). The diathermal transformation results in a destruction of the warmer waters of 3°–4°C ($\overline{G^{\rm sfc}_{\Delta\theta}} = -4.2 \pm 0.3$ Sv) and a formation of the colder waters of 2°–3°C ($\overline{G^{\rm sfc}_{\Delta\theta}} = 2.4 \pm 0.4$ Sv; Fig. 9b). As mentioned in section 4b, these surface-induced volume changes are largely counteracted by those induced by the restratifying eddies, with a small impact on the total thermohaline volume changes. The opposing impacts from surface forcing and mixing are also evident in density coordinates. As shown in Fig. 4b, at isopycnals 27.2–27.6 kg m^{-3}, the light-to-dense transformation in response to surface buoyancy loss is opposed by a dense-to-light transformation induced by mixing.

5. Discussion and conclusions

Using a combination of moored measurements, hydrographic datasets, and atmospheric reanalysis products, we investigate the mean water mass transformation and formation rates with respect to potential density σ_θ and thermohaline (S–θ) coordinates in the Labrador Basin during August 2014–August 2019. Our major conclusions are summarized in Fig. 10.

In σ_θ coordinate, surface buoyancy loss (2.3 ± 0.2 Sv) and diapycnal mixing (1.3 ± 1.2 Sv) collectively lead to a maximum light-to-dense transformation of 3.6 ± 1.2 Sv at 27.7 kg m^{-3} (Fig. 10b). This light-to-dense volume flux is responsible for the volume destruction of 5.0 ± 1.2 Sv in the upper layer (27–27.7 kg m^{-3}) and the volume formation of 4.9 ± 1.5 Sv in the intermediate layer (27.7–27.8 kg m^{-3}) that contains LSW. Importantly, 63% of the formation rate in this intermediate layer is attributed to diapycnal mixing (3.1 ± 1.5 Sv), which transforms waters from both the upper layer (1.3 ± 1.2 Sv) and the overflow layer (1.8 ± 1.0 Sv) into the intermediate layer. The remaining 37% (1.8 ± 0.3 Sv) of the formation rate is accomplished by surface buoyancy loss acting on the convective area in the central-western Labrador Sea. These results highlight the importance of mixing in driving the diapycnal transformation and formation associated with the LSW density layer.

By investigating transformation and formation in S–θ coordinates, we are able to distinguish volume fluxes between water masses having the same density but different temperature and salinity. The most pronounced diathermohaline transformation (~10 Sv) is from the warmer, saltier IW into the colder, fresher ULW and LSW. The transformation is found to primarily occur along constant density surfaces (centered at 27.7 kg m^{-3}) and is attributed to mesoscale activities west of Greenland that efficiently exchange properties between the boundary current and basin interior. This conclusion differs from that of an idealized modeling study, which attributes the diathermohaline transformation to the combined effects of surface flux and mixing within the boundary current system (Bebieva and Lozier 2023). Specifically, using a three-layer model, the authors show that cold anomalies in the boundary current are produced by direct surface heat loss, while fresh anomalies result from mixing with fresh shelf water along the Greenland and Labrador coasts. While it is clear that surface heat loss and fresh shelf water input are ultimately responsible for the cold and fresh anomalies in the basin, how they collectively generate the observed thermohaline structure in the Labrador Sea is unresolved. Given the limits imposed by observational datasets, this resolution might best be accomplished with output from comprehensive ocean models.

In addition, we identify counteractive diathermal volume fluxes induced by surface heat flux and interior mixing.

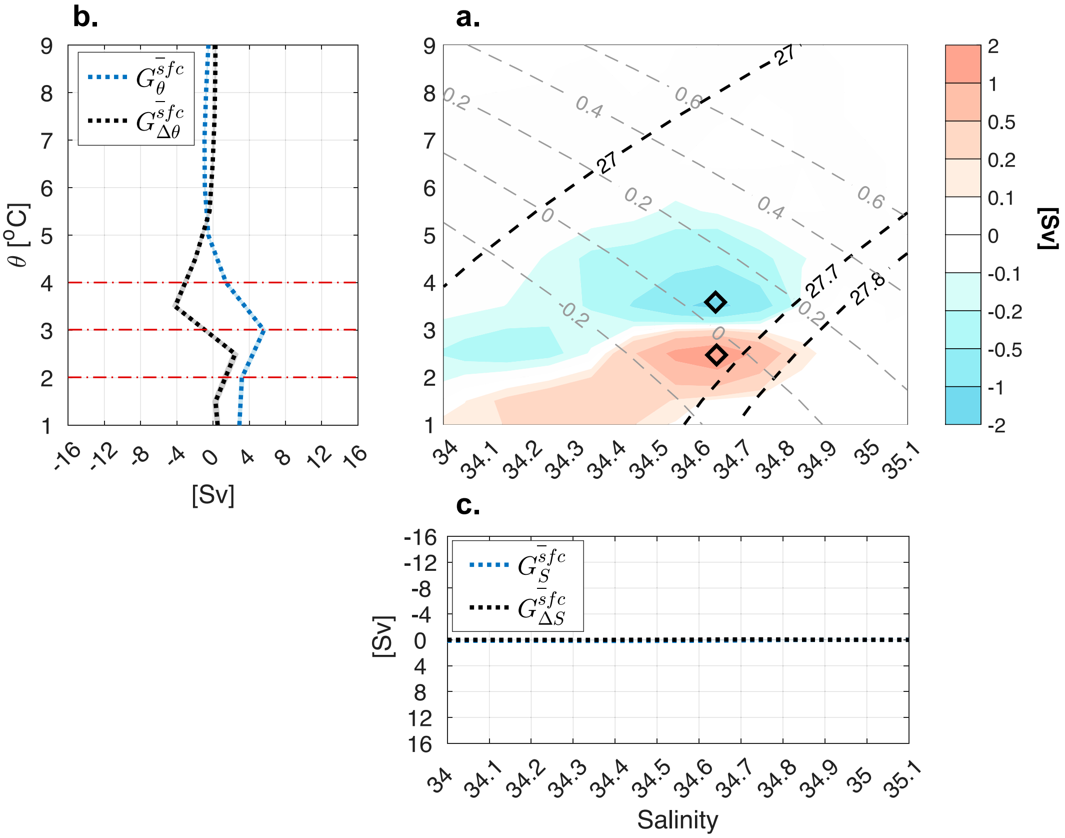

FIG. 9. (a) Mean thermohaline formation rate induced by surface flux $\overline{\nabla_{S\theta}\cdot\mathbf{G}^{\mathrm{sfc}}_{S\theta}}$. Black diamonds denote S–θ bins, i.e., [34.6–34.7, 3°–4°C] and [34.6–34.7, 2°–3°C], where surface-induced volume changes are the strongest. (b) Mean diathermal transformation $\overline{G^{\mathrm{sfc}}_{\theta}}$ (dotted blue) and formation $\overline{G^{\mathrm{sfc}}_{\theta}}$ (dotted black) in response to surface heat flux. Horizontal red dashed lines denote isotherms of 2°, 3°, and 4°C. (c) As in (b), but in S coordinate.

Specifically, surface heat loss results in a warm-to-cold transformation of 5.6 ± 0.3 Sv at 3°C in the southwestern Labrador Sea, which is significantly counteracted by a cold-to-warm transformation induced by mixing surrounding the convective patch. The mixing, which is important for restratifying the mixed layer, is likely associated with the eddies, such as convective eddies and boundary current eddies, and filaments developed at the unstable front along the rim of the convection site.

One caveat of the study is that the contribution from interior mixing is estimated as a residual in the volume budget and its associated physical process is only implied. An explicit quantification of mixing and other unresolved processes in terms of their contributions to the water mass transformation would require further investigations with numerical models. In addition, because the results presented in this study cover a period of intense convection, we are not in a position to understand how they may change during periods of weak convection. While we anticipate similar transformation and formation processes to occur, their magnitudes would likely be smaller (e.g., Myers and Donnelly 2008). Extended OSNAP observations and analyses will yield this answer in time. Finally, we acknowledge that our assumption that the mean transport at the Davis Strait during 2004–10 is representative of the mean during the study period of 2014–19 adds some uncertainty to our results.

Results from this observation-based work, along with those from previous studies, highlight the advantage of viewing water mass changes in thermohaline coordinates. It is shown, from a quantitative perspective, that the thermohaline properties and volumes of the deep-water mass in the Labrador Basin are influenced not only by surface flux but also by mixing that occurs both along and across density surfaces. Our results have important implications for modeling deep-water and AMOC change. First of all, they underscore the necessity to resolve or reasonably parameterize small-scale mixing in the models in order to adequately simulate deep-water properties and formation. Second, the large thermohaline anomalies and their compensating effect on density imply significant impacts from both heat and freshwater forcings in the Labrador Sea. Incorrect representation of either forcing may result in property (especially salinity) biases in climate models, which are directly related to the simulated AMOC strength and its meridional connectivity (Heuzé 2021; Jackson and Petit 2023). Overall, we believe that results from this work provide important observational constraints for modeling deep-water

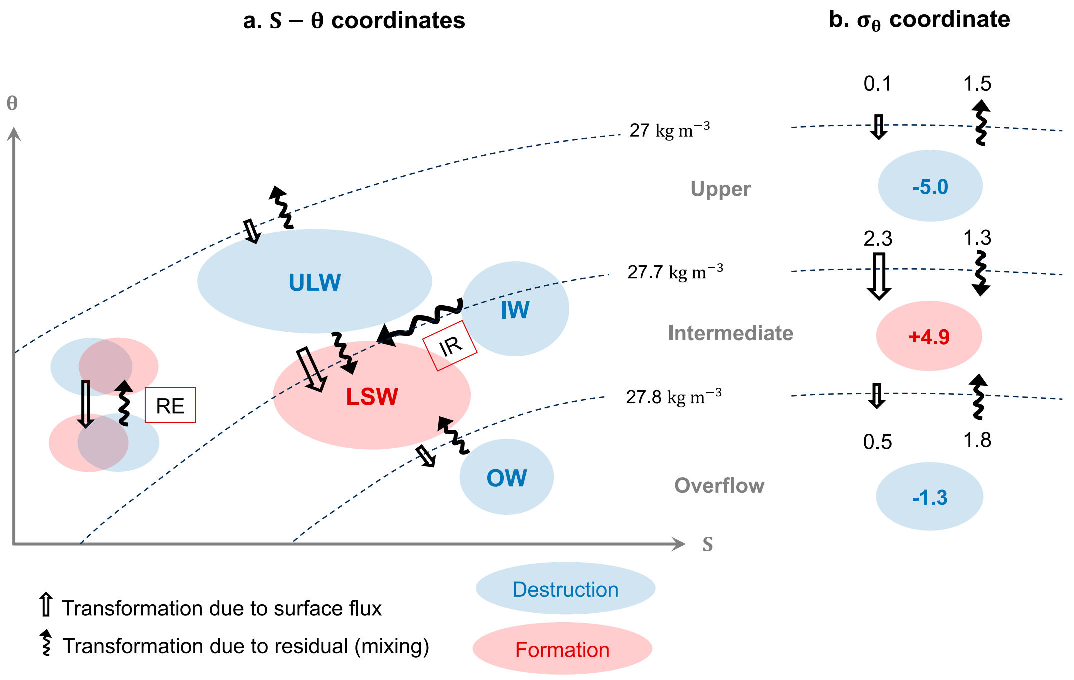

FIG. 10. Schematic of transformation and formation in (a) S–θ coordinates and (b) σ_θ coordinate. IR denotes Irminger Rings, and RE denotes restratifying eddies.

evolution, which is key for predicting the AMOC's response to a warming climate.

Acknowledgments. This work was supported by the National Natural Science Foundation of China (Grant 42376005) and the National Key Research and Development Program of China (2023YFF0805102). T. Petit was supported by the UKRI-NERC SNAP-DRAGON (NE/T013494/1) project. M. S. Lozier acknowledges support from the Physical Oceanography Program of the U.S. National Science Foundation (OCE-1948335). Gratitude is extended to L. Chafik for helpful conversations on the transformation analysis and Y. Fu for tests with OSNAP gridded products. This study has been conducted using E.U. Copernicus Marine Service Information (https://doi.org/10.48670/moi-00052). OSNAP data were collected and made freely available by the OSNAP (Overturning in the Subpolar North Atlantic Program) project and all the national programs that contribute to it (http://www.o-snap.org).

Data availability statement. All data used in this study are publicly available. Gridded data from the OSNAP can be downloaded from https://www.o-snap.org/data-access/. Gridded product at the Davis Strait is downloaded from https://iop.apl.washington.edu/downloads.php. ARMOR3D dataset is accessed at https://doi.org/10.48670/moi-00052. EN4 dataset is accessed at https://www.metoffice.gov.uk/hadobs/en4/download-en4-2-2.html. ISAS dataset is downloaded from https://www.seanoe.org/data/00412/52367/. ERA5 is downloaded from https://www.ecmwf.int/en/forecasts/datasets/reanalysis-datasets/era5. NCEP/NCAR can be accessed at https://www.ncep.noaa.gov. JRA-55 is downloaded from https://rda.ucar.edu/datasets/ds628.1/.

REFERENCES

Badin, G., R. G. Williams, and J. Sharples, 2010: Water-mass transformation in the shelf seas. *J. Mar. Res.*, **68**, 189–214, https://doi.org/10.1357/002224010793721442.

Bebieva, Y., and M. S. Lozier, 2023: Fresh water and atmospheric cooling control on density-compensated overturning in the Labrador Sea. *J. Phys. Oceanogr.*, **53**, 2575–2589, https://doi.org/10.1175/JPO-D-22-0238.1.

Biastoch, A., C. W. Böning, J. Getzlaff, J.-M. Molines, and G. Madec, 2008: Causes of interannual–decadal variability in the meridional overturning circulation of the midlatitude North Atlantic Ocean. *J. Climate*, **21**, 6599–6615, https://doi.org/10.1175/2008JCLI2404.1.

Böning, C. W., F. O. Bryan, W. R. Holland, and R. Döscher, 1996: Deep-water formation and meridional overturning in a high-resolution model of the North Atlantic. *J. Phys. Oceanogr.*, **26**, 1142–1164, https://doi.org/10.1175/1520-0485(1996)026<1142:DWFAMO>2.0.CO;2.

——, P. Wagner, P. Handmann, F. U. Schwarzkopf, K. Getzlaff, and A. Biastoch, 2023: Decadal changes in Atlantic overturning due to the excessive 1990s Labrador Sea convection. *Nat. Commun.*, **14**, 4635, https://doi.org/10.1038/s41467-023-40323-9.

Bracco, A., J. Pedlosky, and R. S. Pickart, 2008: Eddy formation near the west coast of Greenland. *J. Phys. Oceanogr.*, **38**, 1992–2002, https://doi.org/10.1175/2008JPO3669.1.

Brambilla, E., L. D. Talley, and P. E. Robbins, 2008: Subpolar mode water in the northeastern Atlantic: 2. Origin and transformation. *J. Geophys. Res.*, **113**, C04026, https://doi.org/10.1029/2006JC004063.

Brandt, P., A. Funk, L. Czeschel, C. Eden, and C. W. Böning, 2007: Ventilation and transformation of Labrador Sea Water and its rapid export in the deep Labrador Current. *J. Phys. Oceanogr.*, **37**, 946–961, https://doi.org/10.1175/JPO3044.1.

Brüggemann, N., and C. A. Katsman, 2019: Dynamics of downwelling in an eddying marginal sea: Contrasting the Eulerian and the isopycnal perspective. *J. Phys. Oceanogr.*, **49**, 3017–3035, https://doi.org/10.1175/JPO-D-19-0090.1.

Chanut, J., B. Barnier, W. Large, L. Debreu, T. Penduff, J. M. Molines, and P. Mathiot, 2008: Mesoscale eddies in the Labrador Sea and their contribution to convection and restratification. *J. Phys. Oceanogr.*, **38**, 1617–1643, https://doi.org/10.1175/2008JPO3485.1.

Cuny, J., P. B. Rhines, P. P. Niiler, and S. Bacon, 2002: Labrador Sea boundary currents and the fate of the Irminger Sea water. *J. Phys. Oceanogr.*, **32**, 627–647, https://doi.org/10.1175/1520-0485(2002)032<0627:LSBCAT>2.0.CO;2.

Curry, B., C. M. Lee, B. Petrie, R. E. Moritz, and R. Kwok, 2014: Multiyear volume, liquid freshwater, and sea ice transports through Davis Strait, 2004–10. *J. Phys. Oceanogr.*, **44**, 1244–1266, https://doi.org/10.1175/JPO-D-13-0177.1.

Danabasoglu, G., S. G. Yeager, Y.-O. Kwon, J. J. Tribbia, A. S. Phillips, and J. W. Hurrell, 2012: Variability of the Atlantic meridional overturning circulation in CCSM4. *J. Climate*, **25**, 5153–5172, https://doi.org/10.1175/JCLI-D-11-00463.1.

de Boyer Montégut, C., G. Madec, A. S. Fischer, A. Lazar, and D. Iudicone, 2004: Mixed layer depth over the global ocean: An examination of profile data and a profile-based climatology. *J. Geophys. Res.*, **109**, C12003, https://doi.org/10.1029/2004JC002378.

de Jong, M. F., H. M. van Aken, K. Våge, and R. S. Pickart, 2012: Convective mixing in the central Irminger Sea: 2002–2010. *Deep-Sea Res. I*, **63**, 36–51, https://doi.org/10.1016/j.dsr.2012.01.003.

——, A. S. Bower, and H. H. Furey, 2014: Two years of observations of warm-core anticyclones in the Labrador Sea and their seasonal cycle in heat and salt stratification. *J. Phys. Oceanogr.*, **44**, 427–444, https://doi.org/10.1175/JPO-D-13-070.1.

——, ——, and ——, 2016: Seasonal and interannual variations of Irminger ring formation and boundary–interior heat exchange in FLAME. *J. Phys. Oceanogr.*, **46**, 1717–1734, https://doi.org/10.1175/JPO-D-15-0124.1.

——, M. Oltmanns, J. Karstensen, and L. de Steur, 2018: Deep convection in the Irminger Sea observed with a dense mooring array. *Oceanography*, **31** (1), 50–59, https://doi.org/10.5670/oceanog.2018.109.

de Lavergne, C., G. Madec, J. Le Sommer, A. J. G. Nurser, and A. C. N. Garabato, 2016: On the consumption of Antarctic bottom water in the abyssal ocean. *J. Phys. Oceanogr.*, **46**, 635–661, https://doi.org/10.1175/JPO-D-14-0201.1.

Desbruyères, D. G., H. Mercier, G. Maze, and N. Daniault, 2019: Surface predictor of overturning circulation and heat content change in the subpolar North Atlantic. *Ocean Sci.*, **15**, 809–817, https://doi.org/10.5194/os-15-809-2019.

Drinkwater, K. F., 1988: On the mean and tidal currents in Hudson Strait. *Atmos.–Ocean*, **26**, 252–266, https://doi.org/10.1080/07055900.1988.9649302.

Dukhovskoy, D. S., I. Yashayaev, E. P. Chassignet, P. G. Myers, G. Platov, and A. Proshutinsky, 2021: Time scales of the Greenland freshwater anomaly in the subpolar North Atlantic. *J. Climate*, **34**, 8971–8987, https://doi.org/10.1175/JCLI-D-20-0610.1.

Ebita, A., and Coauthors, 2011: The Japanese 55-year reanalysis "JRA-55": An interim report. *SOLA*, **7**, 149–152, https://doi.org/10.2151/sola.2011-038.

Eden, C., and C. Böning, 2002: Sources of eddy kinetic energy in the Labrador Sea. *J. Phys. Oceanogr.*, **32**, 3346–3363, https://doi.org/10.1175/1520-0485(2002)032<3346:SOEKEI>2.0.CO;2.

Evans, D. G., J. D. Zika, A. C. N. Garabato, and A. J. G. Nurser, 2014: The imprint of Southern Ocean overturning on seasonal water mass variability in Drake Passage. *J. Geophys. Res. Oceans*, **119**, 7987–8010, https://doi.org/10.1002/2014JC010097.

——, N. P. Holiday, S. Bacon, and I. Le Bras, 2023: Mixing and air–sea buoyancy fluxes set the time-mean overturning circulation in the subpolar North Atlantic and Nordic Seas. *Ocean Sci.*, **19**, 745–768, https://doi.org/10.5194/os-19-745-2023.

Ferrari, R., A. Mashayek, T. J. McDougall, M. Nikurashin, and J.-M. Campin, 2016: Turning Ocean mixing upside down. *J. Phys. Oceanogr.*, **46**, 2239–2261, https://doi.org/10.1175/JPO-D-15-0244.1.

Fu, Y., and Coauthors, 2023: Seasonality of the meridional overturning circulation in the subpolar North Atlantic. *Commun. Earth Environ.*, **4**, 181, https://doi.org/10.1038/s43247-023-00848-9.

Gaillard, F., T. Reynaud, V. Thierry, N. Kolodziejczyk, and K. von Schuckmann, 2016: In situ–based reanalysis of the global ocean temperature and salinity with ISAS: Variability of the heat content and steric height. *J. Climate*, **29**, 1305–1323, https://doi.org/10.1175/JCLI-D-15-0028.1.

Garcia-Quintana, Y., P. Courtois, X. Hu, C. Pennelly, D. Kieke, and P. G. Myers, 2019: Sensitivity of Labrador Sea water formation to changes in model resolution, atmospheric forcing, and freshwater input. *J. Geophys. Res. Oceans*, **124**, 2126–2152, https://doi.org/10.1029/2018JC014459.

Georgiou, S., S. L. Ypma, N. Brüggemann, J.-M. Sayol, C. G. van der Boog, P. Spence, J. D. Pietrzak, and C. A. Katsman, 2021: Direct and indirect pathways of convected water masses and their impacts on the overturning dynamics of the Labrador Sea. *J. Geophys. Res. Oceans*, **126**, e2020JC016654, https://doi.org/10.1029/2020JC016654.

Good, S. A., M. J. Martin, and N. A. Rayner, 2013: EN4: Quality controlled ocean temperature and salinity profiles and monthly objective analyses with uncertainty estimates. *J. Geophys. Res. Oceans*, **118**, 6704–6716, https://doi.org/10.1002/2013JC009067.

Gou, R., P. Li, K. N. Wiegand, C. Pennelly, D. Kieke, and P. G. Myers, 2023: Variability of eddy formation off the west Greenland coast from a 1/60° model. *J. Phys. Oceanogr.*, **53**, 2475–2490, https://doi.org/10.1175/JPO-D-23-0004.1.

Gouretski, V., and F. Reseghetti, 2010: On depth and temperature biases in bathythermograph data: Development of a new correction scheme based on analysis of a global ocean database. *Deep-Sea Res. I*, **57**, 812–833, https://doi.org/10.1016/j.dsr.2010.03.011.

Grist, J. P., R. Marsh, and S. A. Josey, 2009: On the relationship between the North Atlantic meridional overturning circulation and the surface-forced overturning streamfunction. *J. Climate*, **22**, 4989–5002, https://doi.org/10.1175/2009JCLI2574.1.

——, and Coauthors, 2010: The roles of surface heat flux and ocean heat transport convergence in determining Atlantic Ocean temperature variability. *Ocean Dyn.*, **60**, 771–790, https://doi.org/10.1007/s10236-010-0292-4.

——, S. A. Josey, R. Marsh, Y.-O. Kwon, R. J. Bingham, and A. T. Blaker, 2014: The surface-forced overturning of the North Atlantic: Estimates from modern era atmospheric reanalysis datasets. *J. Climate*, **27**, 3596–3618, https://doi.org/10.1175/JCLI-D-13-00070.1.

Groeskamp, S., J. D. Zika, B. M. Sloyan, T. J. McDougall, and P. C. McIntosh, 2014a: A thermohaline inverse method for estimating diathermohaline circulation and mixing. *J. Phys. Oceanogr.*, **44**, 2681–2697, https://doi.org/10.1175/JPO-D-14-0039.1.

——, ——, T. J. McDougall, B. M. Sloyan, and F. Laliberté, 2014b: The representation of ocean circulation and variability in thermodynamic coordinates. *J. Phys. Oceanogr.*, **44**, 1735–1750, https://doi.org/10.1175/JPO-D-13-0213.1.

——, R. P. Abernathey, and A. Klocker, 2016: Water mass transformation by cabbeling and thermobaricity. *Geophys. Res. Lett.*, **43**, 10 835–10 845, https://doi.org/10.1002/2016GL070860.

——, S. M. Griffies, D. Iudicone, R. Marsh, A. J. G. Nurser, and J. D. Zika, 2019: The water mass transformation framework for ocean physics and biogeochemistry. *Annu. Rev. Mar. Sci.*, **11**, 271–305, https://doi.org/10.1146/annurev-marine-010318-095421.

Guinehut, S., A.-L. Dhomps, G. Larnicol, and P.-Y. Le Traon, 2012: High resolution 3-D temperature and salinity fields derived from in situ and satellite observations. *Ocean Sci.*, **8**, 845–857, https://doi.org/10.5194/os-8-845-2012.

Haine, T., and Coauthors, 2008: North Atlantic deep water formation in the Labrador Sea, recirculation through the subpolar gyre, and discharge to the subtropics. *Arctic–Subarctic Ocean Fluxes*, Springer, 653–701.

Hall, M. M., D. J. Torres, and I. Yashayaev, 2013: Absolute velocity along the AR7W section in the Labrador Sea. *Deep-Sea Res. I*, **72**, 72–87, https://doi.org/10.1016/j.dsr.2012.11.005.

Heuzé, C., 2021: Antarctic bottom water and North Atlantic deep water in CMIP6 models. *Ocean Sci.*, **17**, 59–90, https://doi.org/10.5194/os-17-59-2021.

Jackson, L. C., and T. Petit, 2023: North Atlantic overturning and water mass transformation in CMIP6 models. *Climate Dyn.*, **60**, 2871–2891, https://doi.org/10.1007/s00382-022-06448-1.

Jones, H., and J. Marshall, 1997: Restratification after deep convection. *J. Phys. Oceanogr.*, **27**, 2276–2287, https://doi.org/10.1175/1520-0485(1997)027<2276:RADC>2.0.CO;2.

Kalnay, E., and Coauthors, 1996: The NCEP/NCAR 40-Year Reanalysis Project. *Bull. Amer. Meteor. Soc.*, **77**, 437–472, https://doi.org/10.1175/1520-0477(1996)077<0437:TNYRP>2.0.CO;2.

Khatiwala, S., P. Schlosser, and M. Visbeck, 2002: Rates and mechanisms of water mass transformation in the Labrador Sea as inferred from tracer observations. *J. Phys. Oceanogr.*, **32**, 666–686, https://doi.org/10.1175/1520-0485(2002)032<0666:RAMOWM>2.0.CO;2.

Klocker, A., and T. J. McDougall, 2010: Influence of the nonlinear equation of state on global estimates of dianeutral advection and diffusion. *J. Phys. Oceanogr.*, **40**, 1690–1709, https://doi.org/10.1175/2010JPO4303.1.

Koelling, J., D. W. R. Wallace, U. Send, and J. Karstensen, 2017: Intense oceanic uptake of oxygen during 2014–2015 winter convection in the Labrador Sea. *Geophys. Res. Lett.*, **44**, 7855–7864, https://doi.org/10.1002/2017GL073933.

Lazier, J., R. Hendry, A. Clarke, I. Yashayaev, and P. Rhines, 2002: Convection and restratification in the Labrador Sea, 1990–2000. *Deep-Sea Res. I*, **49**, 1819–1835, https://doi.org/10.1016/S0967-0637(02)00064-X.

LeBel, D. A., and Coauthors, 2008: The formation rate of North Atlantic deep water and eighteen degree water calculated from CFC-11 inventories observed during WOCE. *Deep-Sea Res. I*, **55**, 891–910, https://doi.org/10.1016/j.dsr.2008.03.009.

Li, F., M. S. Lozier, and W. E. Johns, 2017: Calculating the meridional volume, heat and freshwater transports from an observing system in the subpolar North Atlantic: Observing system simulation experiment. *J. Atmos. Oceanic Technol.*, **34**, 1483–1500, https://doi.org/10.1175/JTECH-D-16-0247.1.

——, ——, G. Danabasoglu, N. P. Holliday, Y.-O. Kwon, A. Romanou, S. G. Yeager, and R. Zhang, 2019: Local and downstream relationships between Labrador Sea water volume and North Atlantic meridional overturning circulation variability. *J. Climate*, **32**, 3883–3898, https://doi.org/10.1175/JCLI-D-18-0735.1.

——, and Coauthors, 2021: Subpolar North Atlantic western boundary density anomalies and the meridional overturning circulation. *Nat. Commun.*, **12**, 3002, https://doi.org/10.1038/s41467-021-23350-2.

Li, P., R. Chen, R. Gou, C. Pennelly, Y. Luo, and P. G. Myers, 2023: Winter mixed layer restratification induced by vertical eddy buoyancy flux in the Labrador Sea. *Geophys. Res. Lett.*, **50**, e2023GL103341, https://doi.org/10.1029/2023GL103341.

Lilly, J. M., P. B. Rhines, F. Schott, K. Lavender, J. Lazier, U. Send, and E. D'Asaro, 2003: Observations of the Labrador Sea eddy field. *Prog. Oceanogr.*, **59**, 75–176, https://doi.org/10.1016/j.pocean.2003.08.013.

Lozier, M. S., and Coauthors, 2019: A sea change in our view of overturning in the subpolar North Atlantic. *Science*, **363**, 516–521, https://doi.org/10.1126/science.aau6592.

——, A. S. Bower, H. H. Furey, K. L. Drouin, X. Xu, and S. Zou, 2022: Overflow water pathways in the North Atlantic. *Prog. Oceanogr.*, **208**, 102874, https://doi.org/10.1016/j.pocean.2022.102874.

Iudicone, D., G. Madec, and T. J. McDougall, 2008: Water-mass transformations in a neutral density framework and the key role of light penetration. *J. Phys. Oceanogr.*, **38**, 1357–1376, https://doi.org/10.1175/2007JPO3464.1.

MacGilchrist, G. A., H. L. Johnson, D. P. Marshall, C. Lique, M. Thomas, L. C. Jackson, and R. A. Wood, 2020: Locations and mechanisms of ocean ventilation in the high-latitude North Atlantic in an eddy-permitting ocean model. *J. Climate*, **33**, 10 113–10 131, https://doi.org/10.1175/JCLI-D-20-0191.1.

Mackay, N., C. Wilson, J. Zika, and N. P. Holliday, 2018: A regional thermohaline inverse method for estimating circulation and mixing in the Arctic and subpolar North Atlantic. *J. Atmos. Oceanic Technol.*, **35**, 2383–2403, https://doi.org/10.1175/JTECH-D-17-0198.1.

——, ——, N. P. Holliday, and J. D. Zika, 2020: The observation-based application of a regional thermohaline inverse method to diagnose the formation and transformation of water masses north of the OSNAP array from 2013 to 2015. *J. Phys. Oceanogr.*, **50**, 1533–1555, https://doi.org/10.1175/JPO-D-19-0188.1.

Marsh, R., 2000: Recent variability of the North Atlantic thermohaline circulation inferred from surface heat and freshwater fluxes. *J. Climate*, **13**, 3239–3260, https://doi.org/10.1175/1520-0442(2000)013<3239:RVOTNA>2.0.CO;2.

——, S. A. Josey, A. J. G. de Nurser, B. A. Cuevas, and A. C. Coward, 2005: Water mass transformation in the North Atlantic over 1985–2002 simulated in an eddy-permitting model. *Ocean Sci.*, **1**, 127–144, https://doi.org/10.5194/os-1-127-2005.

Marshall, J., and F. Schott, 1999: Open-ocean convection: Observations, theory, and models. *Rev. Geophys.*, **37** (1), 1–64, https://doi.org/10.1029/98RG02739.

McCartney, M. S., 1992: Recirculating components to the deep boundary current of the northern North Atlantic. *Prog. Oceanogr.*, **29**, 283–383, https://doi.org/10.1016/0079-6611(92)90006-L.

McDougall, T. J., 1987: Thermobaricity, cabbeling, and water-mass conversion. *J. Geophys. Res.*, **92**, 5448–5464, https://doi.org/10.1029/JC092iC05p05448.

Mulet, S., M.-H. Rio, A. Mignot, S. Guinehut, and R. Morrow, 2012: A new estimate of the global 3D geostrophic ocean circulation based on satellite data and in-situ measurements. *Deep-Sea Res. II*, **77–80**, 70–81, https://doi.org/10.1016/j.dsr2.2012.04.012.

Myers, P. G., and C. Donnelly, 2008: Water mass transformation and formation in the Labrador Sea. *J. Climate*, **21**, 1622–1638, https://doi.org/10.1175/2007JCLI1722.1.

Nicolas, K., P.-M. Annaig, and G. Fabienne, 2021: ISAS temperature and salinity gridded fields. SEANOE, accessed 16 July 2021, https://doi.org/10.17882/52367.

Pacini, A., and Coauthors, 2020: Mean conditions and seasonality of the West Greenland boundary current system near Cape Farewell. *J. Phys. Oceanogr.*, **50**, 2849–2871, https://doi.org/10.1175/JPO-D-20-0086.1.

Palter, J. B., M. S. Lozier, and K. L. Lavender, 2008: How does Labrador Sea water enter the deep western boundary current? *J. Phys. Oceanogr.*, **38**, 968–983, https://doi.org/10.1175/2007JPO3807.1.

Pennelly, C., and P. G. Myers, 2020: Introducing LAB60: A 1/60° NEMO 3.6 numerical simulation of the Labrador Sea. *Geosci. Model Dev.*, **13**, 4959–4975, https://doi.org/10.5194/gmd-13-4959-2020.

Pérez, F. F., H. Mercier, M. Vázquez-Rodríguez, P. Lherminier, A. Velo, P. C. Pardo, G. Rosón, and A. F. Ríos, 2013: Atlantic Ocean CO_2 uptake reduced by weakening of the meridional overturning circulation. *Nat. Geosci.*, **6**, 146–152, https://doi.org/10.1038/ngeo1680.

Petit, T., M. S. Lozier, S. A. Josey, and S. A. Cunningham, 2020: Atlantic deep water formation occurs primarily in the Iceland basin and Irminger Sea by local buoyancy forcing. *Geophys. Res. Lett.*, **47**, e2020GL091028, https://doi.org/10.1029/2020GL091028.

Pickart, R. S., and M. A. Spall, 2007: Impact of Labrador Sea convection on the North Atlantic meridional overturning circulation. *J. Phys. Oceanogr.*, **37**, 2207–2227, https://doi.org/10.1175/JPO3178.1.

——, ——, and J. R. N. Lazier, 1997: Mid-depth ventilation in the western boundary current system of the sub-polar gyre. *Deep-Sea Res. I*, **44**, 1025–1054, https://doi.org/10.1016/S0967-0637(96)00122-7.

——, D. J. Torres, and R. A. Clarke, 2002: Hydrography of the Labrador Sea during active convection. *J. Phys. Oceanogr.*, **32**, 428–457, https://doi.org/10.1175/1520-0485(2002)032<0428:HOTLSD>2.0.CO;2.

——, F. Straneo, and G. W. K. Moore, 2003: Is Labrador Sea water formed in the Irminger basin? *Deep-Sea Res. I*, **50**, 23–52, https://doi.org/10.1016/S0967-0637(02)00134-6.

Piron, A., V. Thierry, H. Mercier, and G. Caniaux, 2017: Gyre-scale deep convection in the subpolar North Atlantic Ocean during winter 2014–2015. *Geophys. Res. Lett.*, **44**, 1439–1447, https://doi.org/10.1002/2016GL071895.

Poli, P., and Coauthors, 2016: ERA-20C: An atmospheric reanalysis of the twentieth century. *J. Climate*, **29**, 4083–4097, https://doi.org/10.1175/JCLI-D-15-0556.1.

Rhein, M., and Coauthors, 2002: Labrador Sea water: Pathways, CFC inventory, and formation rates. *J. Phys. Oceanogr.*, **32**, 648–665, https://doi.org/10.1175/1520-0485(2002)032<0648:LSWPCI>2.0.CO;2.

Ridenour, N. A., F. Straneo, J. Holte, Y. Gratton, P. G. Myers, and D. G. Barber, 2021: Hudson strait inflow: Structure and variability. *J. Geophys. Res. Oceans*, **126**, e2020JC017089, https://doi.org/10.1029/2020JC017089.

Rieck, J. K., C. W. Böning, and K. Getzlaff, 2019: The nature of eddy kinetic energy in the Labrador Sea: Different types of mesoscale eddies, their temporal variability, and impact on deep convection. *J. Phys. Oceanogr.*, **49**, 2075–2094, https://doi.org/10.1175/JPO-D-18-0243.1.

Rühs, S., E. C. J. Oliver, A. Biastoch, C. W. Böning, M. Dowd, K. Getzlaff, T. Martin, and P. G. Myers, 2021: Changing spatial patterns of deep convection in the subpolar North Atlantic. *J. Geophys. Res. Oceans*, **126**, e2021JC017245, https://doi.org/10.1029/2021JC017245.

Sabine, C. L., and Coauthors, 2004: The oceanic sink for anthropogenic CO_2. *Science*, **305**, 367–371, https://doi.org/10.1126/science.1097403.

Smethie, W. M., Jr., and R. A. Fine, 2001: Rates of North Atlantic deep water formation calculated from chlorofluorocarbon inventories. *Deep-Sea Res. I*, **48**, 189–215, https://doi.org/10.1016/S0967-0637(00)00048-0.

Speer, K., and E. Tziperman, 1992: Rates of water mass formation in the North Atlantic Ocean. *J. Phys. Oceanogr.*, **22**, 93–104, https://doi.org/10.1175/1520-0485(1992)022<0093:ROWMFI>2.0.CO;2.

Speer, K. G., H.-J. Isemer, and A. Biastoch, 1995: Water mass formation from revised COADS data. *J. Phys. Oceanogr.*, **25**, 2444–2457, https://doi.org/10.1175/1520-0485(1995)025<2444:WMFFRC>2.0.CO;2.

Tagklis, F., A. Bracco, T. Ito, and R. M. Castelao, 2020: Submesoscale modulation of deep water formation in the Labrador Sea. *Sci. Rep.*, **10**, 17489, https://doi.org/10.1038/s41598-020-74345-w.

Talley, L. D., and M. S. McCartney, 1982: Distribution and circulation of Labrador Sea water. *J. Phys. Oceanogr.*, **12**, 1189–1205, https://doi.org/10.1175/1520-0485(1982)012<1189:DACOLS>2.0.CO;2.

Thornalley, D. J. R., and Coauthors, 2018: Anomalously weak Labrador Sea convection and Atlantic overturning during the past 150 years. *Nature*, **556**, 227–230, https://doi.org/10.1038/s41586-018-0007-4.

Walin, G., 1982: On the relation between sea-surface heat flow and thermal circulation in the ocean. *Tellus*, **34A**, 187–195, https://doi.org/10.3402/tellusa.v34i2.10801.

Xu, X., P. B. Rhines, E. P. Chassignet, and W. J. Schmitz Jr., 2015: Spreading of Denmark strait overflow water in the western subpolar North Atlantic: Insights from eddy-resolving simulations with a passive tracer. *J. Phys. Oceanogr.*, **45**, 2913–2932, https://doi.org/10.1175/JPO-D-14-0179.1.

——, ——, and ——, 2018: On mapping the diapycnal water mass transformation of the upper North Atlantic Ocean. *J. Phys. Oceanogr.*, **48**, 2233–2258, https://doi.org/10.1175/JPO-D-17-0223.1.

Yashayaev, I., 2007: Hydrographic changes in the Labrador Sea, 1960–2005. *Prog. Oceanogr.*, **73**, 242–276, https://doi.org/10.1016/j.pocean.2007.04.015.

——, and J. W. Loder, 2017: Further intensification of deep convection in the Labrador Sea in 2016. *Geophys. Res. Lett.*, **44**, 1429–1438, https://doi.org/10.1002/2016GL071668.

Yeager, S., and Coauthors, 2021: An outsized role for the Labrador Sea in the multidecadal variability of the Atlantic overturning circulation. *Sci. Adv.*, **7**, eabh3592, https://doi.org/10.1126/sciadv.abh3592.

Zhang, R., R. Sutton, G. Danabasoglu, Y.-O. Kwon, R. Marsh, S. G. Yeager, D. E. Amrhein, and C. M. Little, 2019: A review of the role of the Atlantic meridional overturning circulation in Atlantic multidecadal variability and associated climate impacts. *Rev. Geophys.*, **57**, 316–375, https://doi.org/10.1029/2019RG000644.

Zou, S., M. S. Lozier, F. Li, R. Abernathey, and L. Jackson, 2020a: Density-compensated overturning in the Labrador Sea. *Nat. Geosci.*, **13**, 121–126, https://doi.org/10.1038/s41561-019-0517-1.

——, A. Bower, H. Furey, M. S. Lozier, and X. Xu, 2020b: Redrawing the Iceland–Scotland overflow water pathways in the North Atlantic. *Nat. Commun.*, **11**, 1890, https://doi.org/10.1038/s41467-020-15513-4.